BAMS Article

The Great Plains Irrigation Experiment (GRAINEX)

Eric Rappin, Rezaul Mahmood, Udaysankar Nair, Roger A. Pielke Sr., William Brown, Steve Oncley, Joshua Wurman, Karen Kosiba, Aaron Kaulfus, Chris Phillips, Emilee Lachenmeier, Joseph Santanello Jr., Edward Kim, and Patricia Lawston-Parker

ABSTRACT: Extensive expansion in irrigated agriculture has taken place over the last half century. Due to increased irrigation and resultant land-use–land-cover change, the central United States has seen a decrease in temperature and changes in precipitation during the second half of the twentieth century. To investigate the impacts of widespread commencement of irrigation at the beginning of the growing season and continued irrigation throughout the summer on local and regional weather, the Great Plains Irrigation Experiment (GRAINEX) was conducted in the spring and summer of 2018 in southeastern Nebraska. GRAINEX consisted of two 15-day intensive observation periods. Observational platforms from multiple agencies and universities were deployed to investigate the role of irrigation in surface moisture content, heat fluxes, diurnal boundary layer evolution, and local precipitation. This article provides an overview of the data collected and an analysis of the role of irrigation in land–atmosphere interactions on time scales from the seasonal to the diurnal. The analysis shows that a clear irrigation signal was apparent during the peak growing season in mid-July. This paper shows the strong impact of irrigation on surface fluxes, near-surface temperature and humidity, and boundary layer growth and decay.

KEYWORDS: Atmosphere-land interaction; Soil moisture

https://doi.org/10.1175/BAMS-D-20-0041.1
Corresponding author: Rezaul Mahmood, rmahmood2@unl.edu
Supplemental material: https://doi.org/10.1175/BAMS-D-20-0041.2

In final form 20 April 2021

AFFILIATIONS: Rappin—Department of Geography and Geology, and Kentucky Climate Center, Western Kentucky University, Bowling Green, Kentucky; **Mahmood and Lachenmeier**—High Plains Regional Climate Center, School of Natural Resources, University of Nebraska–Lincoln, Lincoln, Nebraska; **Nair, Kaulfus, and Phillips**—Department of Atmospheric Science, University of Alabama in Huntsville, Huntsville, Alabama; **Pielke**—Department of Atmospheric and Oceanic Sciences, and Cooperative Institute for Research in Environmental Sciences, University of Colorado Boulder, Boulder, Colorado; **Brown and Oncley**—Earth Observation Laboratory, National Center for Atmospheric Research, Boulder, Colorado; **Wurman and Kosiba**—Center for Severe Weather Research, Boulder, Colorado; **Santanello and Kim**—NASA Goddard Space Flight Center, Greenbelt, Maryland; **Lawston-Parker**—Earth System Science Interdisciplinary Center, University of Maryland, College Park, College Park, and NASA Goddard Space Flight Center, Greenbelt, Maryland

Land-use–land-cover changes (LULCCs) play an important role in modulating weather and climate [National Research Council (NRC); NRC 2005; Pielke et al. 2011; Mahmood et al. 2010, 2014; Pielke et al. 2016]. Evidence of its importance can be found in the Third National Climate Assessment (Melillo et al. 2014), Coupled Model Intercomparison Project 5 (CMIP5) in support of the Fifth Assessment of Climate Change by the IPCC (e.g., Brovkin et al. 2013), Land-Use and Climate, Identification of robust impacts (LUCID) experiments (Pitman et al. 2009), and from the inclusion of LULCC in preparation of CMIP6 (Meehl et al. 2014) in support of the Sixth Assessment.

Observations and modeling studies suggest that LULCC impacts meso-, regional-, and potentially global-scale atmospheric circulations, temperature, precipitation, and fluxes (e.g., Segal et al. 1989; Gero et al. 2006; Costa et al. 2007; Campra et al. 2008; Puma and Cook 2010; Davin and de Noblet-Ducoudré 2010; NRC 2012; He et al. 2020; Thiery et al. 2020; Chen et al. 2020). In line with these results, it has been found that agriculture and irrigation significantly impact weather and climate (e.g., Puma and Cook 2010; Sen Roy et al. 2011; Wei et al. 2013; Lawston et al. 2020). In an observational study, Sen Roy et al. (2011) reported up to a 69-mm increase in dry-season precipitation in the irrigated regions of northwestern India. Based on a modeling study with global focus, Wei et al. (2013) noted a ~120-mm increase in annual precipitation in South Asia because of irrigation. Lawston et al. (2020) found a 1.67°C cooling of mean temperatures in the central part of Washington, United States, during summer due to irrigation. Excellent examples of irrigation impacts can be found in the Great Plains (GP) of North America (Barnston and Schickedanz 1984; Mahmood and Hubbard 2002; Adegoke et al. 2003; DeAngelis et al. 2010; Lawston et al. 2015; Szilagyi and Franz 2020). Barnston and Schickedanz (1984) have shown from observational data that irrigation increases precipitation in the southern Great Plains. In a follow-up and more detailed study DeAngelis et al. (2010) have also shown that irrigation in the Great Plains impacts precipitation as far as in Indiana and in Kentucky (downwind impact). Mahmood and Hubbard (2002) have conducted a model-based climatological research and found 36% increase in growing-season physical evaporation and transpiration (Miralles et al. 2020) due to irrigation and resulted in a >1°C lowering of mean maximum growing-season temperature during the second half of the twentieth century over the northern Great Plains. In a subsequent study, Adegoke et al. (2003) have found similar changes in latent heat fluxes over irrigated areas of Nebraska and further verified previous results.

The irrigated region of the GP extends from Texas to Nebraska and some of the most widespread applications of irrigation can be found in Nebraska (Mahmood and Hubbard 2002). Due to the extent of the GP region, commencement of irrigation each year depends on the start of the growing season, which is influenced by local climate and weather in the preceding several months. For example, in the northern part of the GP (northern plains), irrigation typically begins in the latter part of May (e.g., Mahmood and Hubbard 2002).

Commencement of irrigation and its impact on regional hydrometeorology is like a *binary switch* in the Great Plains. Irrigated landscape goes from no irrigation [lower soil moisture (SM)] to fully operational irrigation (higher SM). This switch can occur rapidly over a few days to slightly over a week for areas from a few square kilometers to a few thousand square kilometers, respectively. We suggest that impacts on land surface condition, land–atmosphere (L-A) interactions (e.g., Santanello et al. 2018), and the resultant evolution of the boundary layer in and around irrigated areas are significant. Application of irrigation reaches its maximum in July and early August during the plant vegetative growth stage when plant-water requirements are at their highest levels. These intraseasonal changes impact meso- and regional-scale thermodynamic fields (Mahmood et al. 2004, 2008).

Recent work has further supported the need for field campaigns. Gerken et al. (2019) reported that feedbacks between precipitation and land surface fluxes including physical evaporation and transpiration are difficult to observe, but critical for understanding the role of the land surface in the Earth system. As noted previously, in Asia, Sen Roy et al. (2011) reported an increase in dry-season rainfall in northwestern India due to irrigation. Devanand et al. (2019) discussed an increase in extreme rainfall in central India in recent decades, and that irrigation increases the rainfall intensity during these events. Their study concluded that it is important to represent irrigation practices more accurately in climate models. Nikiel and Eltahir (2019) reported that a combination of agricultural development and decadal variability of global sea surface temperatures (SST) explains most of the observed variability of summer temperature and precipitation during the twentieth century over central North America.

Despite prior research showing significant potential of irrigated land cover to impact weather, observational campaigns investigating such land–atmosphere interactions are lacking. This paper discusses initial results from such an observational study that investigated the impacts of irrigation on the diurnal evolution of the planetary boundary layer (PBL), cloud development, and precipitation during a field data collection campaign undertaken in southeastern Nebraska. The overall study is known as the Great Plains Irrigation Experiments (GRAINEX) (www.eol.ucar.edu/field_projects/grainex). The overarching research goal is to assess *how irrigation, compared to absence of irrigation, impacts boundary layer development, precipitation, and its various characteristics*. The results discussed in this paper will improve our understanding of L-A interactions particularly in the context of LULCC and widespread applications of irrigation. Multiweek continuous data collection, analyses of field measurements, and modeling provided further insights into L-A interactions. All data analyzed in this study are quality controlled.

Data were collected during the growing season of 2018 in collaboration with the Earth Observation Laboratory's (EOL's) Lower Atmospheric Observation Facilities (LAOF) of the National Center for Atmospheric Research (NCAR), the Center for Severe Weather Research (CSWR), and the Environmental Monitoring, Economical Sensor Hubs (EMESH) system of the University of Alabama in Huntsville. Field data collection efforts included radar wind profilers, radiosonde observations, eddy covariance flux stations, mobile radars known as Doppler on Wheels (DOW), and a dense surface meteorological network (Fig. 1; details in the following section). In addition, the National Aeronautics and Space Administration (NASA) joined this effort. They have collected data using sensors mounted on a Twin Otter aircraft and further contributed to this study.

Two recent field campaigns, the Soil Moisture–Atmosphere Coupling Experiment (SMACEX) (Kustas et al. 2005) and the International H_2O Project (IHOP_2002) (Weckwerth et al. 2004) addressed L-A interactions. In addition, Koster et al. (2004) identified the GP as a "hotspot" of L-A interactions. However, despite the importance and global expansion of irrigation due to ever-increasing demand for food, these field campaigns and resulting studies did not directly address the role of irrigation in GP weather and L-A interactions. Further, current

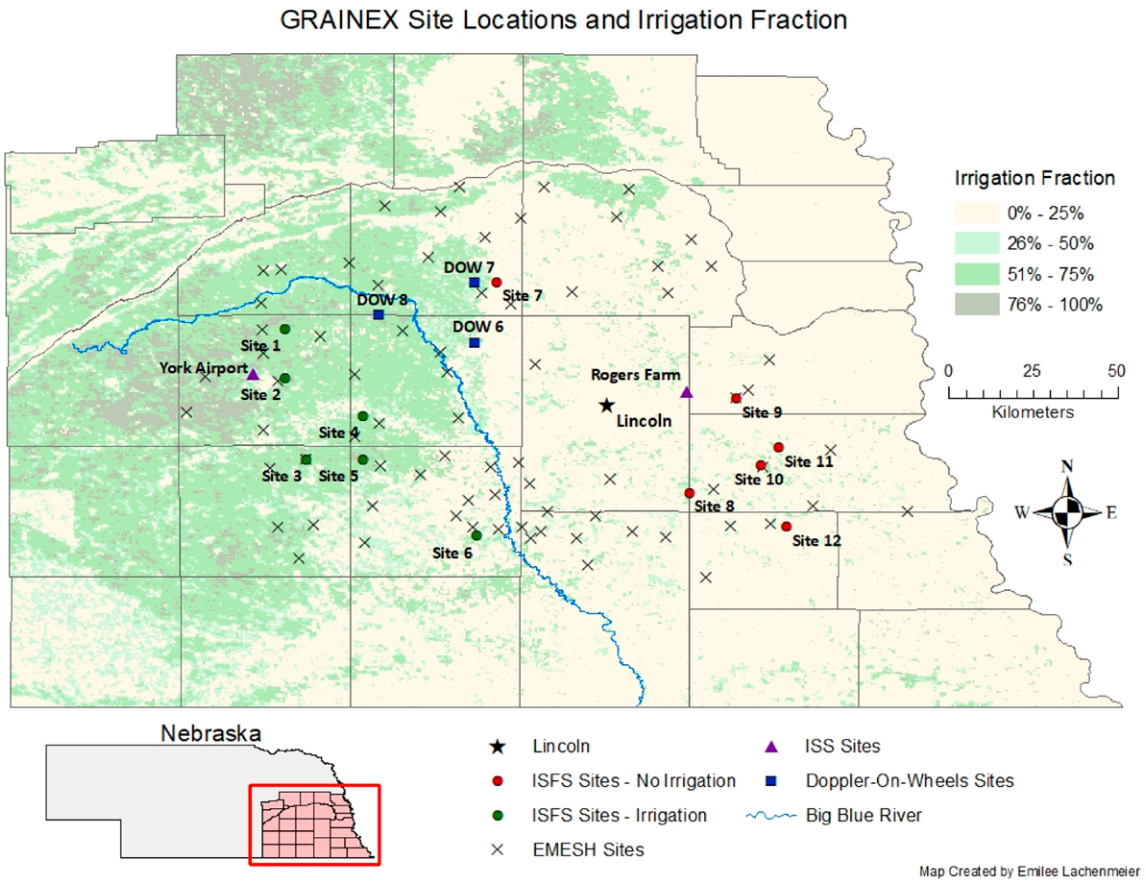

Fig. 1. Locations of various observation platforms over eastern Nebraska. The region transitions from nonirrigated (in the east) to irrigated (in the west) areas.

irrigation schemes in Earth system models are rather primitive, and reliant on assumptions about irrigation practices that lack an observational basis (Lawston et al. 2017). We also suggest that GRAINEX is the first experiment of this type, a highly focused project specifically designed to collect data over contrasting and adjacent irrigated and nonirrigated regions to study irrigation impacts. Due to the uncertain role of irrigation impacts on precipitation, the results presented here make a fundamental contribution to that aspect of L-A interactions.

Field experiment overview and data collection

The GRAINEX field campaign took place in southeastern Nebraska over a ~100 km × 100 km area comprised of adjacent irrigated and nonirrigated land from the end of May until the beginning of August (Fig. 1). Nebraska was selected as it is one of the most highly irrigated regions of the world, and the most irrigated state of the United States. The Big Blue River in southeastern Nebraska separates extensively irrigated croplands to the west and nonirrigated cropland to the east (Fig. 1).

Two intensive-observation periods (IOPs) were selected with a much more extensive observational array (as discussed below) for 1) 29 May–13 June 2018 (IOP1) and 2) 16–30 July 2018 (IOP2). IOP1dates were chosen to capture the commencement of irrigation, or *binary switch*, during which there is a rapid change in moisture availability occur. IOP2 dates were selected to investigate land–atmosphere interactions at the height of the growing season when crop-water demand and irrigation applications are also at a maximum.

Observational platforms include Integrated Surface Flux System (ISFS), Integrated Sounding System (ISS), radiosondes, DOW, and EMESH (Figs. 2a–h). Details of the observations can be found in www.eol.ucar.edu/field_projects/grainex. These details include, among others,

description of instrumentation and data quality. Below we provide a brief description of these observation platforms and their deployment design.

ISFS. To determine irrigation impacts, six ISFS (UCAR/NCAR 1990) were deployed over irrigated and six ISFS over nonirrigated areas (Figs. 1, 2a–d and Table 1). All of the irrigated ISFS sites are located over the western part of the study area, while nonirrigated sites are over the eastern part. As can be found from Table 1, all sites measured standard above surface meteorological

Fig. 2. (a) An irrigated ISFS tower (site 1 in Fig. 1) at the beginning of the IPO1 with a center-pivot irrigation system in the background, (b) a tripod with net radiometer during IOP1, (c) same ISFS tower but for IOP2 (middle of the growing season), (d) net radiometer during IOP2 (middle of the growing season), (e) ISS radar wind profiler, (f) a launched radiosonde balloon, (g) one of the three Doppler on Wheels (DOW), and (h) an EMESH station next to an irrigated field.

Table 1. GRAINEX ISFS sites and their locations.

Site	Nearest town	Lat (°N)	Lon (°W)	Land use–land cover	Flux sensor mounting height (m)
1	Benedict	41.009 669	97.541 247	Irrigated	6
2	York	40.879 614	97.541 887	Irrigated	6
3	Exeter	40.662 28	97.4846	Irrigated	6
4	Beaver Crossing	40.778 54	97.331 73	Irrigated	6
5	Friend	40.662 223	97.333 542	Irrigated	6
6	Wilber	40.458 504	97.028 949	Irrigated	6
7	Loma	41.135 725	96.974 423	Nonirrigated	4.5
8	Panama	40.573 74	96.461 773	Nonirrigated	6.5
9	Elmwood	40.8238	96.335 17	Nonirrigated	6.5
10	Unadilla	40.645 905	96.271 274	Nonirrigated	6.5
11	Unadilla	40.6932	96.223 161	Nonirrigated	4.5
12	Cook	40.483 095	96.202 562	Nonirrigated	5.5

variables, including, temperature, pressure, relative humidity, rainfall, wind speed and direction, and solar radiation. These sites also measured fluxes of momentum as well as sensible and latent heat at a rate of 50 samples per second. To complete measurements, each site recorded soil moisture, soil temperature, soil heat capacity, and soil heat flux (Table 2). While all sites were operational continuously from about mid-May to mid-August, the ISS and DOWs were only available during the IOPs. As a result, focus is given to these periods. ISFS data were communicated in near–real time via cell modem to EOL/LAOF. These data subsequently went through quality control checks and were delivered as 5-min-average observations.

ISS. Two ISS (UCAR/NCAR 1997) sites were instrumented to help understand the response of PBL to land surface conditions (irrigated versus nonirrigated) (Figs. 1 and 2e). One of these sites was located over an open area at York airport away from runaway and clutter. This small county airport is located just outside of York, Nebraska, and surrounded by extensively irrigated crop fields. A second site was located in Rogers Memorial Farm (short: Rogers Farm), Nebraska, east of Lincoln, Nebraska (Table 3a), representing the nonirrigated region of eastern Nebraska. Both sites included radar wind profiler, ceilometer, and standard surface meteorological observations (Table 3b). Additionally, both sites simultaneously launched radiosondes every 2 h from sunrise [~0500 local standard time (~1100 UTC); there is a 6-h lag in local standard time compared to UTC (LST = UTC – 0600)] to sunset [~1900 local standard

Table 2. Parameters measured at each GRAINEX ISFS sites.

Parameter	Sensor	Mounting height/depth (m)
Air temperature, relative humidity	NCAR TRH	2
Air pressure	Vaisala PTB220, PTB2010 barometers; Paroscientific nanobarometer	2
Fluxes of momentum, sensible and latent heat, and carbon dioxide	Campbell CSAT3A/EC150	4.5–6
Horizontal wind speed amd direction	Gill WindObserver 2D sonic anemometer	10
Precipitation (rain)	MRI tipping bucket	2
Radiation (four components)	Hukseflux NR01 integrated radiometer	2
Soil heat capacity	Hukseflux TP01	–0.025
Soil heat flux	REBS HFT	–0.05
Soil moisture	Decagon EC-5	–0.025
Soil temperature profile	NCAR Tsoil	–0–0.05

time (~0100 UTC)] resulting in eight launches per site per day (Fig. 2f). The data were collected for both IOP1 and IOP2. In short, a comprehensive set of data were collected to understand properties and evolution of the boundary layer during the IOPs over irrigated and nonirrigated regions of the study domain. These observations were also complementary to ISFS observations.

DOW. Three X-band DOW (Wurman 2001) were deployed in a configuration that allowed for data to be collected over irrigated, nonirrigated, and over irrigated to nonirrigated transition zones (Figs. 1 and 2g) to further capture fine-scale evolution of the PBL (Wurman et al. 2021; Wurman and Kosiba 2020). DOW reflectivity and Doppler velocity fields were used to identify atmospheric boundaries in the PBL. These observations were used in conjunction with the other observations in this paper. In addition, the radar data will be used in the future to further investigate the impact of irrigation on PBL development and convective processes. From the three DOW locations, radiosondes (Graw DFM-09) were launched simultaneously in coordination with the ISS sites. Thus, there were about 40 launches per day from the five locations (~1,200 total for two IOPs.) to sample the atmosphere and the evolution of the PBL.

Table 3a. Location of ISS sites.

Site	Description	Lat (°N)	Lon (°W)
ISS2	Rogers Memorial Farm	40.8444	96.4683
ISS3	York Municipal Airport	40.8916	97.6261

Table 3b. Measurements at the ISS locations (Rogers Memorial Farm and York Municipal Airport).

System	Measurement	Sensor
Upper air		
	Cloud height	Vaisala CL31 and CL51 ceilometer
	Sounding variables	Vaisala MW41/RS 41 radiosondes
	Wind profile	LAP3000 915-MHz DBS radar wind profiler with RASS
Surface		
	Pressure	Vaisala PTB210
	Radiation (4 components)	Hukseflux NR01
	Precipitation (rain)	HAS tipping bucket
	Meteorological summary	Lufft WS700/800 weather sensors
	Temperature	
	Relative humidity	
	Precipitation type	
	Precipitation intensity	
	Precipitation quantity	
	Air pressure	
	Wind direction	
	Wind speed	
	Radiation	

EMESH. To further complement these observations and to better capture small-scale surface and near-surface variations, a network of 75 meteorological stations known as EMESH were deployed from late May 2018 through mid-August 2018 covering both IOPs (Figs. 1, 2h and Table 4). EMESH are rapidly deployable weather stations that were developed at the University of Alabama in Huntsville. For this research project, 28 stations were deployed over irrigated

Table 4. Measured parameters at each EMESH station during the GRAINEX.

Parameter	Sensor	Mounting height/depth (m)
Air temperature	BOSCH BMP 180, Sensirion SHT 75	2
Barometric pressure	BOSCH BMP 180	2
Relative humidity	Sensirion SHT 75	2
Wind speed	Davis Vantage Pro 2	3
Wind direction	Davis Vantage Pro 2	3
Rainfall	Sparkfun tipping rain gauge	2
Soil temperature	Maxim DS18B20	−0.05, −0.3
Volumetric soil moisture	METER Group EC-5	−0.05, −0.3

and 47 over nonirrigated areas. Of these 75 stations, 50 and 25 were deployed during the IOP1 and IOP2, respectively. They were successfully field tested for their accuracy and reliability prior to the deployment for this project. Each of these stations recorded standard meteorological parameters as well as soil moisture and temperature (Table 4). This paper does not include analysis of EMESH data.

NASA GREX instrument. The Goddard Radio Frequency Explorer (GREX) microwave (L-band) radiometer was mounted on the NASA Twin Otter plane and was utilized during the IOP2, conducting seven flights from 16 through 27 July 2018 measuring radiances at a spatial resolution < 1 km. The GREX mission was to measure spatial patterns and transects of soil moisture across and between the ground stations. GREX, coupled with a suitable antenna, measures brightness temperature similar to that of the Soil Moisture Active Passive (SMAP) satellite. For GRAINEX, the L-band front-end operated within a 1,400–1,427-MHz frequency range as is utilized by the SMAP radiometer. GREX was set up to match SMAP's single-channel soil moisture algorithm inputs for the GRAINEX deployment. The motivation for flying GREX was to observe spatial surface heterogeneity over the GRAINEX domain and to connect with point-based soil moisture measurements and their variability across the region. Results from GREX data are not included in this paper.

Results

Overall weather conditions during IOP1 and IOP2. During IOP1 eastern Nebraska was on the southern edge of the polar jet, which was comparatively far south for the time of year (Archer and Caldeira 2008; Pielke 2018). The position of the jet resulted in several occurrences of rain from mesoscale convective systems forced by upper-level troughs. The overall result of this pattern were several rain events and occasional cooler and drier days after the cold fronts passed. The synoptic weather pattern during IOP2 was similar to IOP1. Thus, there were extended sunny and partly sunny periods punctuated by showers and thunderstorms.

Surface meteorological conditions. Key quantities including 2-m temperature, mixing ratio, and soil moisture at the ISFS sites, averaged over irrigated (blue) and nonirrigated (red) cropland sites are shown in Figs. 3a–c. All of these observations are recorded at 5-min intervals and then averaged. IOP1 and IOP2 were during the first and last two weeks, respectively, and displayed in the panels. The differences in temperature, mixing ratio, and soil moisture between irrigated and nonirrigated land uses are shown on the right axis of Figs. 3a–c. To minimize the noise of the seasonal figures, the difference calculations are only done at a single time each day, the time of maximum temperature, as averaged over irrigated or nonirrigated cropland. While this does eliminate any response lag between the two croplands, it captures an overall seasonal characteristics.

The 2-m temperature and mixing ratio (Figs. 3a,b) reveal that there were two distinct observed near-surface weather conditions. During IOP1 and prior to 1 July, on average, there was only a relatively smaller observed difference in temperature and mixing ratio between irrigated and nonirrigated croplands. In contrast, during IOP2 and the month of July, as expected, there was a much larger observed difference between irrigated and nonirrigated croplands. During this period, on average, the mean daily temperature over irrigated areas was reduced by −0.69°C because of increased physical evaporation from soils and transpiration from crops. This is reflected in an increased mixing ratio of +1.54 g kg^{-1}.

GRAINEX was also designed to investigate the *binary switch* of the onset and subsequent sustained irrigation on near-surface meteorology and L-A interactions. Due to frequent weather events during IOP1 and much of June, the *binary switch* did not occur until the beginning of July. The large-scale forcing (online supplementary Figs. ES1a–c; https://doi.org/10.1175/BAMS-D-20-0041.2) can be observed in the near-surface meteorology shown in Figs. 3a–c, which

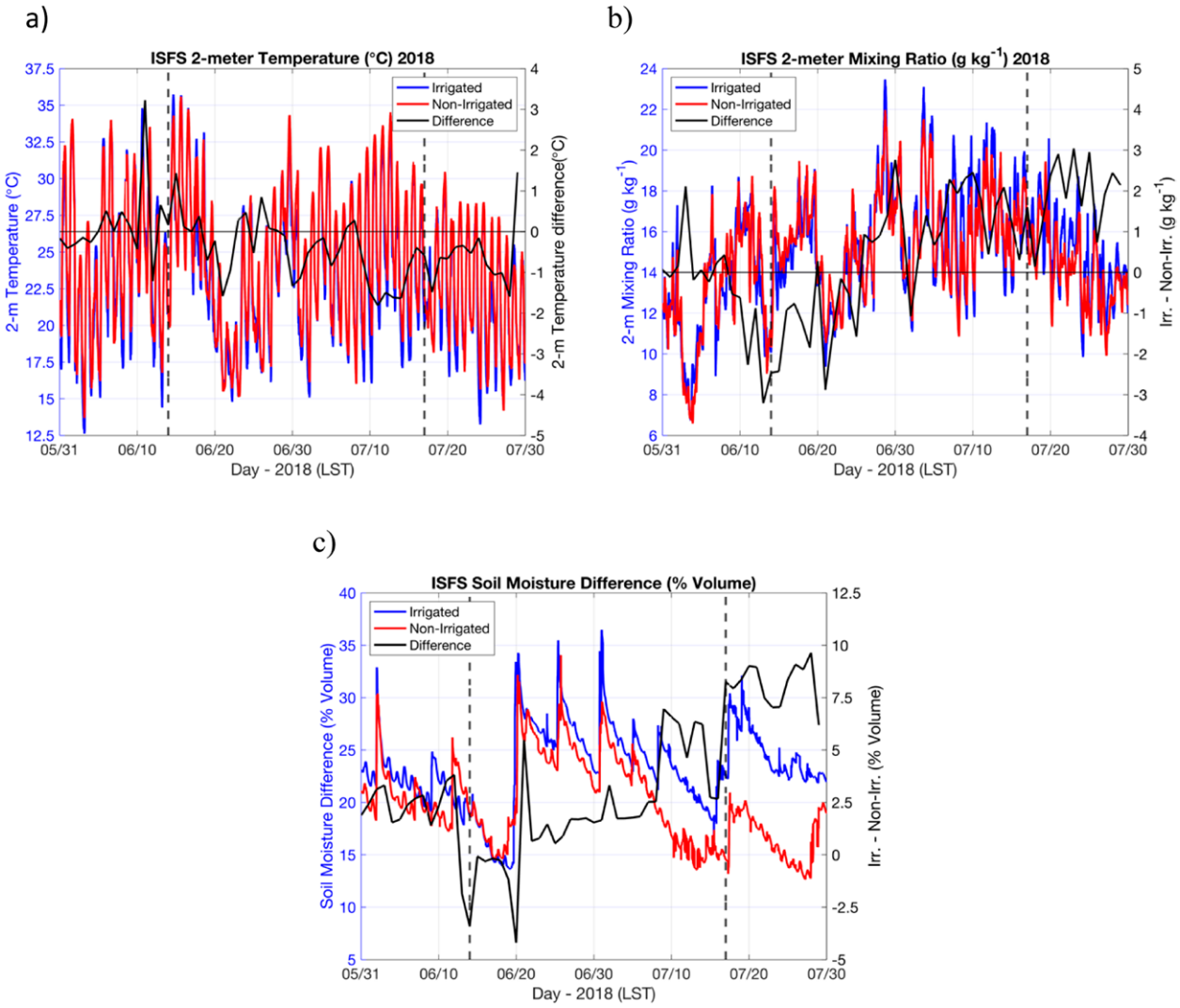

Fig. 3. Average 2-m (a) temperature, (b) mixing ratio, and (c) soil moisture for irrigated and nonirrigated ISFS sites with their differences at the time of their respective daily maximum temperature. These panels included IOP1, IOP2, and the period in between IOP1 and IOP2 (time between two dashed vertical lines). Horizontal line represents zero difference between irrigated and nonirrigated sites.

displays frequent large-amplitude fluctuations in the temperature (Fig. 3a) and mixing ratio (Fig. 3b) suggestive of frontal passages on weekly time scales.

Closer inspection of Fig. 3a reveals a small downward trend in the difference in mean maximum temperature (statistically significant at the 99% confidence level) between the irrigated and nonirrigated sites from mid-June through late July. The downward trend would be expected under an irrigation signal during the growing season. It is because latent heat fluxes dominate energy partition over irrigated areas (please see "Surface fluxes" section below for further details). The 2-m mixing ratio shows a relatively clear response to irrigation with larger values over irrigated cropland (Fig. 3b). In addition, volumetric soil moisture content displayed in Fig. 3c shows the impact of precipitation and irrigation, or lack thereof. While it is difficult to isolate the relative roles, there were clear irrigation signals on 8 July (blue spike in the absence of a red spike) and 24–27 July and light precipitation over irrigated cropland on 23 July.

Due to the observed delay in irrigation onset, IOP1 will be discussed in a rather limited fashion. Attention will be given to IOP2, in particular for the L-A interactions from 22 to 24 July.

Surface fluxes. Data from ISFS sites over irrigated and nonirrigated sites were analyzed for IOP1 and IOP2. Analyses and comparisons are completed for 5-, 15-, and 30-min flux data

and it is found that the results are quite similar (supplementary Figs. ES2a–d). Thus, since this paper presents initial results and overview of the GRAINEX, 5 min data are used. It is evident from Figs. 4a–f that, overall, the latent heat fluxes were higher compared to the sensible heat fluxes during both IOP1 and IOP2. During the early growing-season (IOP1) differences between latent and sensible heat fluxes were not as large as IOP2. However, during peak-growing-season (IOP2) water consumption is higher by plants and the resultant application of irrigation caused increased partitioning of the available energy into the latent heat fluxes. For example, Fig. 4a shows that during the early growing season (IOP1), latent heat fluxes were mainly lower (Figs. 4a,b) over irrigated sites. Frequent changes in weather accompanied by cloud cover suppressed overall heat fluxes. On the other hand, during peak-growing season (IOP2), latent heat fluxes were mostly greater over the same locations. As noted in the previous

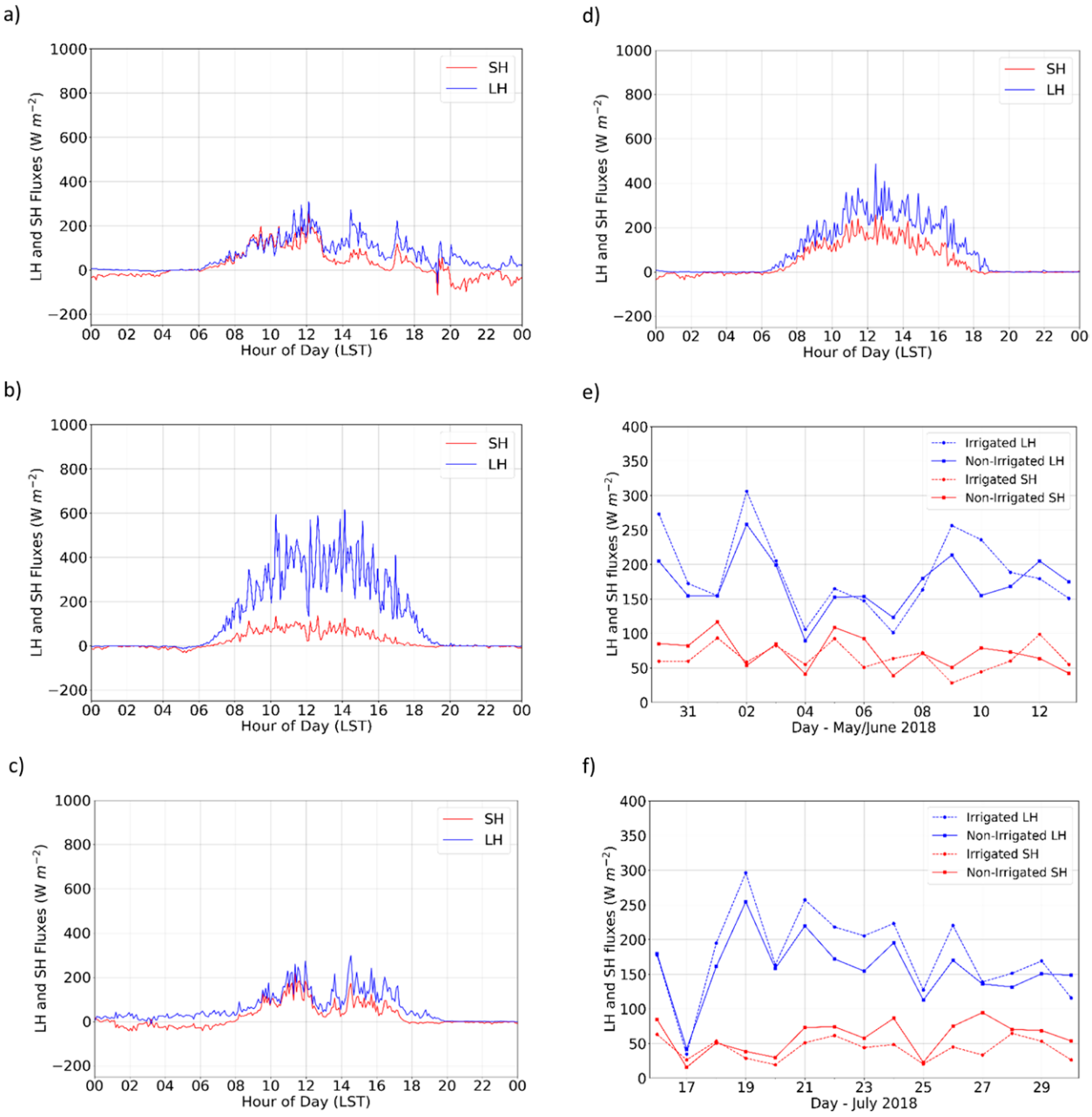

Fig. 4. ISFS irrigated site 1 diurnal variation of surface fluxes for a select date during (a) IOP1 (6 Jun) and (b) IOP2 (24 Jul). (c),(d) As in (a) and (b), but for nonirrigated ISFS site 8 on 7 Jun and 24 Jul, respectively. Daily averaged latent and sensible heat fluxes are for all irrigated and nonirrigated sites: (e) IOP1 and (f) IOP2. To capture fluxes during sunrise to sunset and to synchronize with radiosonde launches, daily averages were calculated for a period from 0500 to 1900 LST.

section and above, synoptic weatherwise IOP1 was more active which depressed fluxes in both irrigated and nonirrigated locations. In addition, Figs. 4e–f also show that on average for all sites, latent (sensible) heat fluxes were consistently higher (lower) during the second IOP2.

There were noticeable decreases in temperature and increases in mixing ratio over irrigated areas, particularly during the last 10 days of IOP2 (Figs. 5a–f). In addition, during the entire month of July, near-surface temperatures were found to be approximately 1°C cooler while

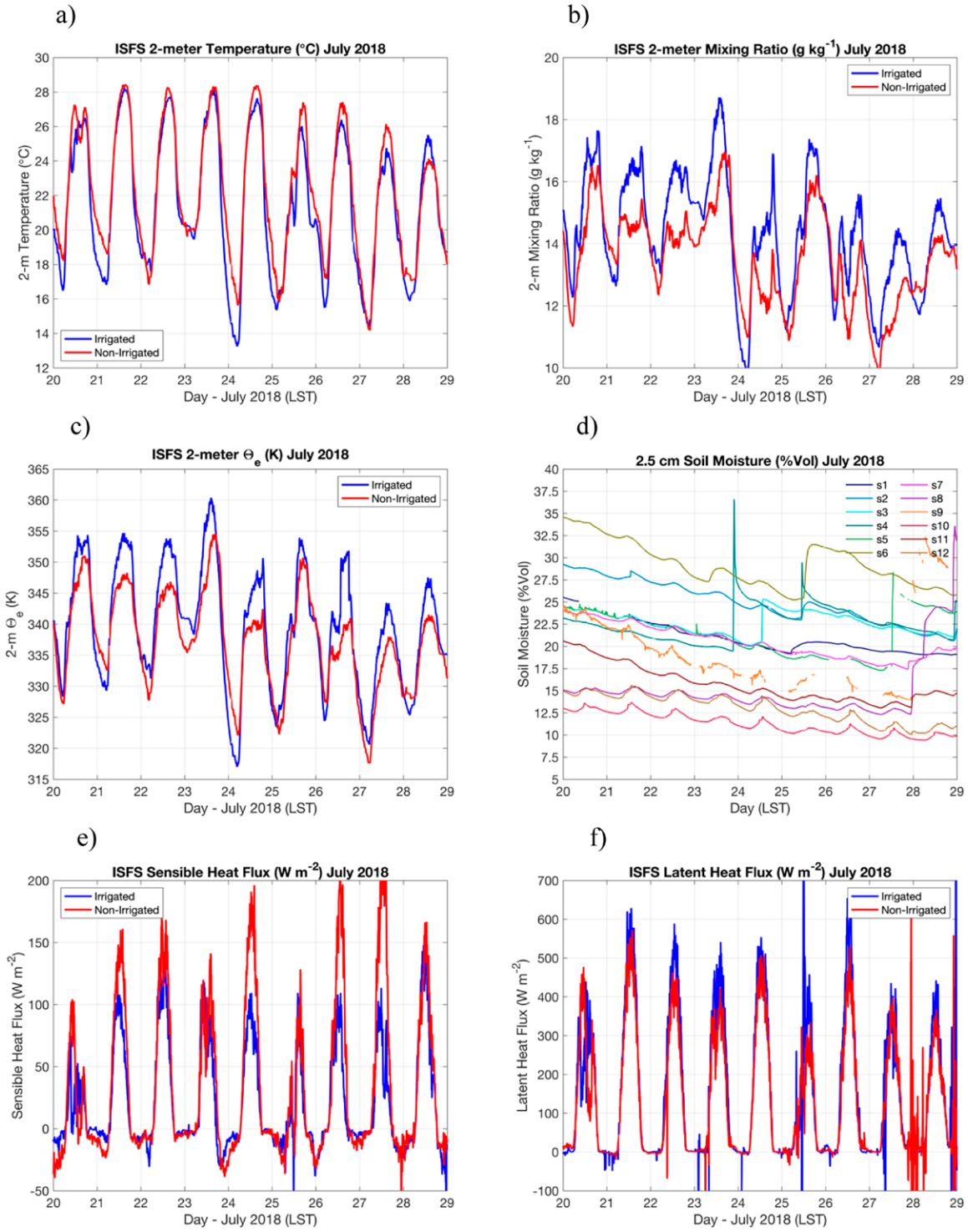

Fig. 5. Average [except for (d)] (a) temperature, (b) mixing ratio, (c) equivalent potential temperature, (d) soil moisture for each ISFS site, (e) sensible heat flux, and (f) latent heat flux over irrigated and nonirrigated ISFS sites during IOP2. In (d), irrigated sites 1–6 are shown as s1–s6 with bluish colors to show higher soil moisture, while nonirrigated sites 7–12 are shown as s7–s12 with reddish colors to show lower soil moisture.

near-surface humidity are 2 g kg^{-1} moister for irrigated land use (cf. with black curves in Fig. 3). Since the moisture contribution was significantly large, equivalent potential temperature (θ_e) increased over irrigated cropland. This result is borne out in Fig. 5c where the near-surface θ_e shows an increase over irrigated land use relative to nonirrigated. Note that, compared to irrigated areas, there were small time lags in reaching the maximum mixing ratio and θ_e over nonirrigated areas (Figs. 5b,c). In the morning, boundary layer evolution was quite similar at all locations with the rapid growth of surface fluxes and boundary layer height through midmorning (~1000 LST). After this time, temperatures rose at a lower rate over irrigated land use as opposed to nonirrigated due to higher soil moisture over irrigated areas. Moreover, we suggest that as latent heat fluxes increased rapidly over irrigated areas, highest values were reached slightly earlier over irrigated land use compared to nonirrigated land use. This particularly reflected in mixing ratio and θ_e values.

Examination of the 2.5-cm soil moisture evolution (Fig. 5d) for the last 10 days of IOP2 shows the diurnal variability and increases due to precipitation and irrigation. Note that the irrigated sites have larger soil moisture values reflective of irrigation prior to and during IOP2. Irrigation applications occur in response to crop-water requirements and soil moisture status and linked to its distribution between field capacity (higher limit) and wilting point (lower limit). As expected, farmers typically do not wait until soil moisture reaching the wilting point and hence soil moisture for irrigated croplands typically varies between field capacity and wilting point. During GRAINEX, the noted differences in near-surface temperature, mixing ratio, and 2.5-cm soil moisture are associated with the observed surface sensible and latent heat fluxes (Figs. 5e–f). In the absence of cloud cover, the sensible heat fluxes increase while the latent heat fluxes decrease at the nonirrigated ISFS sites. In short, compared to nonirrigated locations, higher latent heat fluxes from the irrigated locations lowered temperature and increased θ_e and mixing ratio. On the other hand, sensible heat fluxes dominated over nonirrigated area resulting in higher temperature and lower mixing ratio.

During the first half of the 20–29 July period (IOP2), the near-surface daily maximum temperature remained unchanged near 28°C over irrigated sites while nonirrigated sites were on average about 1°C warmer (Fig. 5a). Due to predominantly clear conditions and higher soil moisture over irrigated areas, physical evaporation and transpiration depleted the soil moisture more rapidly over irrigated sites than over nonirrigated sites (Fig. 5d). The near-surface mixing ratio also decreased (Fig. 5b) due to dry-air advection from the north. Sensible heating increased over the first 5 days as a result of fair weather except for 23 July, which brought overcast conditions and light precipitation to the boundary between irrigated and nonirrigated croplands. Latent heat fluxes decreased across the study area as soil moisture was depleted. However, there was a rebound late on 23 and 24 July after the light rains. The second half of the IOP2 displayed periods of heavier precipitation over irrigated sites on 25 July (primarily at site 6 but also at sites 1 through 4) and on 27 July (site 1) and nonirrigated sites on 28 July (most sites). Overcast conditions lowered surface fluxes on 25 July except for the physical evaporation that occurred after heavy rainfall over irrigated sites. The lack of precipitation led to large sensible heat fluxes over nonirrigated sites until precipitation arrived on 28 July. At this point the sensible heating and temperature were lowered while the latent heating increased.

In contrast to the northerly flow that dominated late July, during the inter-IOP period of early July, deep tropospheric ridging occurred and L-A interactions are expected to dominate. Figures 6a–d display the near-surface temperature, mixing ratio, and surface energy fluxes during the week of 5–12 July. Warm southerly flow dominated the boundary layer during this time leading to increases in temperature and evaporative demand resulting in the applications of irrigation. An example of irrigation can be found at site 6, where on 8 July the volumetric soil moisture nearly doubled from 20% to 40% (not shown). Since there was no precipitation but positive changes in soil moisture, we suggest applications of irrigation

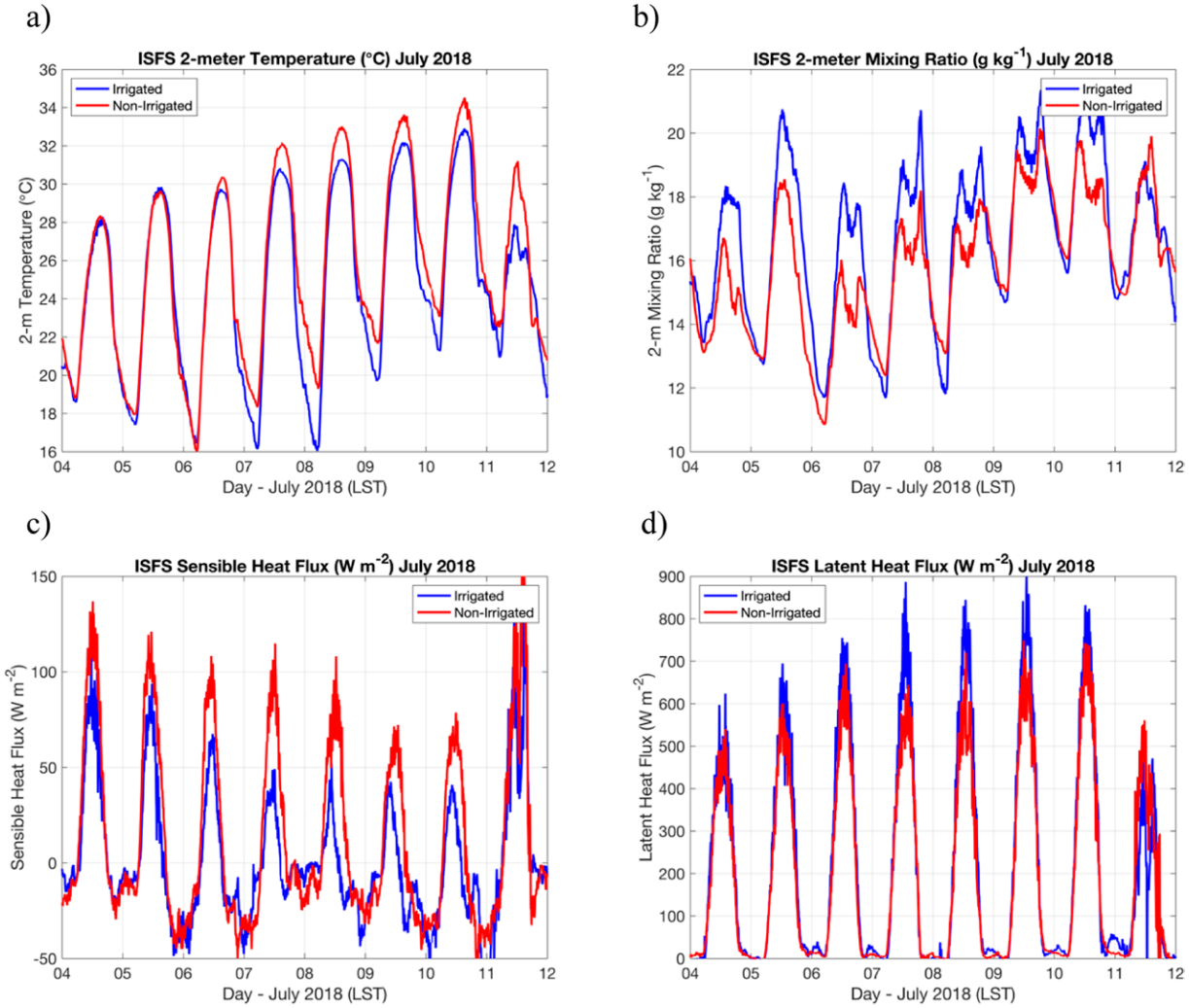

Fig. 6. Average (a) 2-m temperature, (b) 2-m mixing ratio, (c) sensible heat flux, and (d) latent heat flux for irrigated and nonirrigated ISFS sites during the *inter-IOP* period.

played a role in this change. These applications resulted in 2°C-cooler temperatures over irrigated sites compared to nonirrigated sites. In this context, we suggest that the average latent heat flux over irrigated cropland was higher relative to that over nonirrigated cropland due to the irrigation applied on 8 July. With southerly flow and increasing temperature, evaporative demand also increased resulting in higher latent heat fluxes and near-surface mixing ratios. Due to synoptic-scale high pressure settings and weak winds, on a number of nights there were dual maximum in mixing ratio which is not uncommon. One such peak in mixing ratio occurred just prior to the peak in latent heating. Note that after the sunrise the atmospheric boundary layer becomes unstable with further solar radiation leading to development of convection and mixing down of dry air above the inversion in the atmosphere and subsequent lowering of the mixing ratio. In the late afternoon, as sun angle lowers and longwave radiation becomes dominant over incoming shortwave radiation, the convective boundary layer decouples from the surface, and the nighttime inversion layer begins to form. The latter traps any residual physical evaporation and transpiration and leads to late afternoon to evening maximum.

Diurnal observations of 22–24 July 2018

Synoptic evolution. To further understand irrigated and nonirrigated differences, we focus on a 3-day period of 22–24 July 2018 during which two L-A interaction case days occurred and

were separated by a day of weak large-scale ascent and light precipitation. To investigate the L-A interactions in adjacent irrigated and nonirrigated cropland during the 3-day period, three datasets are utilized: 1) ISFS observations of near-surface temperature, dewpoint temperature, soil moisture, accumulated precipitation, and surface fluxes at each site; 2) ISS wind profiler data of wind speed, wind direction, and signal-to-noise ratio at both the York (irrigated) and Rogers Farm (nonirrigated) sites; and 3) ISS radiosonde data of potential temperature, virtual potential temperature, and skew *T* diagrams at both sites.

The synoptic setting with plots of the surface and 300-hPa analyses from the NOAA Storm Prediction Center are shown in Figs. 7a–f for 1800 LST 22 July (0000 UTC 23 July) and 0600 LST 23 July (1200 UTC 23 July) and 1800 LST 23 July (0000 UTC 24 July). At 300 hPa, the GRAINEX domain was between a large stationary high pressure system centered in the southwest United States and a negatively tilted trough in the eastern United States that extended from Minnesota to the Florida Panhandle. By the end of the period on 24 July, the flow was largely zonal as the northern flank of the southeastern high expanded with the eastward propagation of the Canadian low.

During the morning and early afternoon of 23 July, a cold front moved through the GRAINEX study area with satellite and camera imagery showing persistent overcast conditions (not shown) and fog. While a T-shaped thunderstorm complex developed north of the GRAINEX area, the meridional portion of the complex extends southward east of the area while a new north–south-oriented rainband developed over the irrigated area starting at 0600 LST (Figs. 8a–i). The rain line grew in strength as it slowly propagated across the irrigated cropland and dissipated as it moved over the nonirrigated area (discussed further in the next section). Finally, on 24 July, surface high pressure with clear skies and low wind speeds settled over the GRAINEX area providing ideal conditions for strong L-A interactions.

PBL evolution of 22–24 July 2018 as observed by ISFS, ISS, and DOW. On 22 July, near-surface atmospheric conditions (Figs. 9a–e) over the study area are saturated between 0300 and 0600 LST (Figs. 9a,b). With light winds, radiation fog is evident over the York site from camera images (not shown) that dissipates at sunrise and has completely disappeared due to boundary layer mixing by 0700 LST. The fog/cloud cover over irrigation is also evident from the temperature and dewpoint temperature in Figs. 9a and 9b where they remain steady between 0300 and 0600 LST but continue to fall over the nonirrigated locations. As observed in Fig. 5b, the mean mixing ratio over nonirrigated cropland falls to a lower value than over irrigated cropland. The lower value was likely because of dew formation, as the temperature continued to fall, along with the dewpoint, at a faster rate over nonirrigated cropland (Figs. 9a,b). The fog (dew) over irrigated (nonirrigated) cropland is further reflected in the negative sensible heat fluxes between 0300 and 0600 LST (Fig. 9e) as the surface warmed by increasing net radiation. Sites 6 and 7 were located along the irrigation–nonirrigation boundary (Fig. 1) and took on characteristics of both types of land uses. For example, site 7 (pink), a nonirrigated site, displayed the diurnal temperature characteristics of the irrigated sites.

There was no precipitation on 22 July and the largest soil moisture values were found at the irrigated locations (Fig. 9c). The sensible and latent heat fluxes for each site on 22 July are shown in Figs. 9d and 9e. Once the sky was cloud-free, between 0600 and 0700 LST, the air and dewpoint temperatures quickly rose in association with the increases in sensible and latent heat fluxes, respectively. In addition, the fluxes began to reflect the land surface wetness between 1000 and 1500 LST when sensible heat flux decreased and latent heat flux increased. It is during these times when the air and dewpoint temperature also started to diverge between the two different types of land uses (Figs. 9a,b).

Figures 10a–d display the wind speed and wind direction at both ISS sites on 22 July. Light winds dominated the boundary layer outside of a near-surface wind maxima around

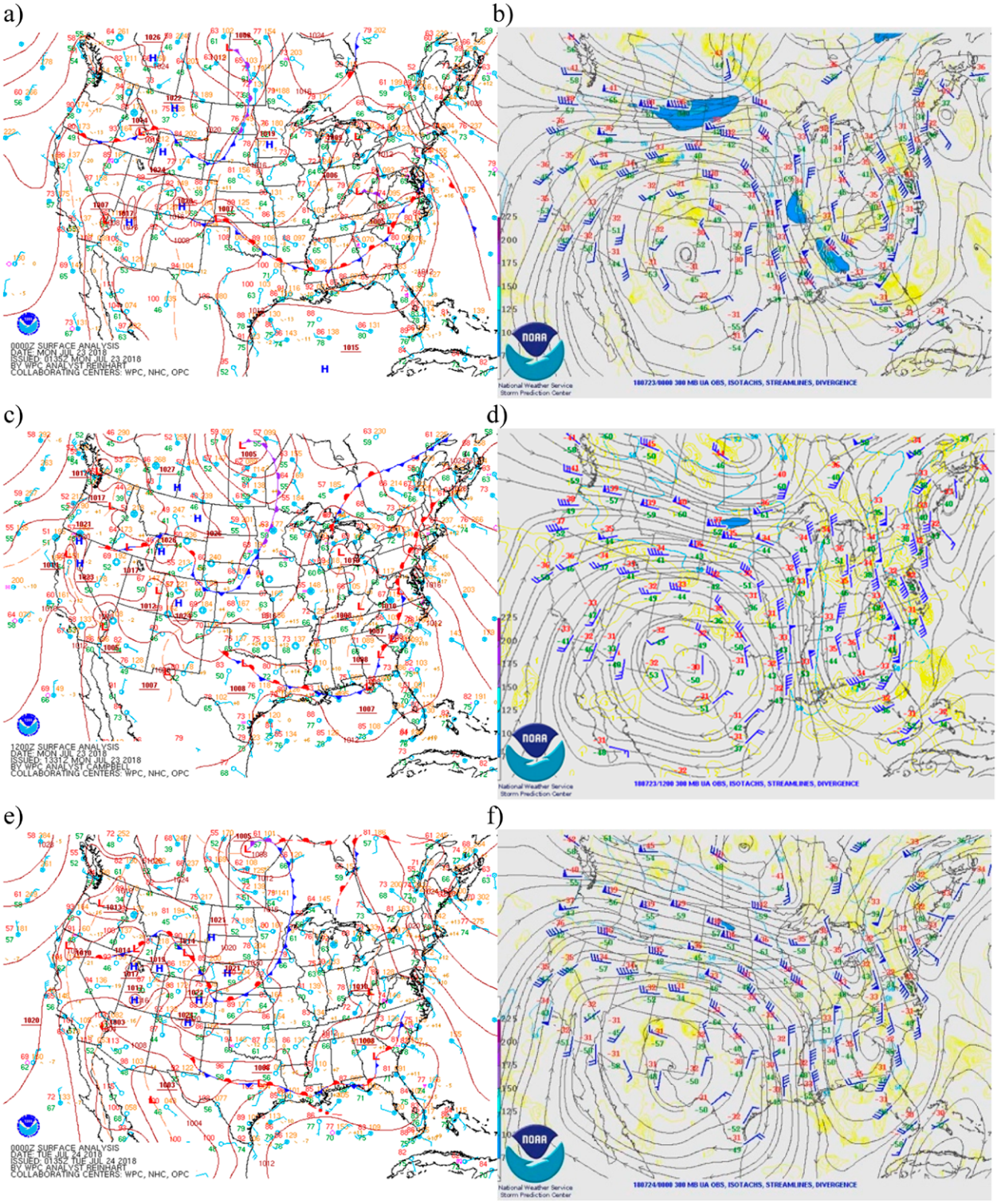

Fig. 7. Synoptic-scale conditions over the conterminous United States provided by NOAA's Weather Prediction Center and Storm Prediction Center. (left) Surface analyses and (right) 300-hPa analyses at (a),(b) 1800 LST 22 Jul (0000 UTC 23 Jul) 2018, (c),(d) 0600 LST (1200 UTC) 23 Jul 2018, and (e),(f) 1800 LST 23 Jul (0000 UTC 24 Jul) 2018. In the right column, blue shaded areas and yellow lines show jet streaks and divergence, respectively.

250 m that formed around late evening and did not subside until sunrise. Above the boundary layer, stronger winds persisted over Rogers Farm as a cold front approached York from the west. Rogers Farm area was under the influence of stronger pressure gradient compared to York and northwest flow that existed above the boundary layer. Conversely, the flow aloft became westerly and diffluent over York. After sunrise, the PBL height (PBLH) increased, as

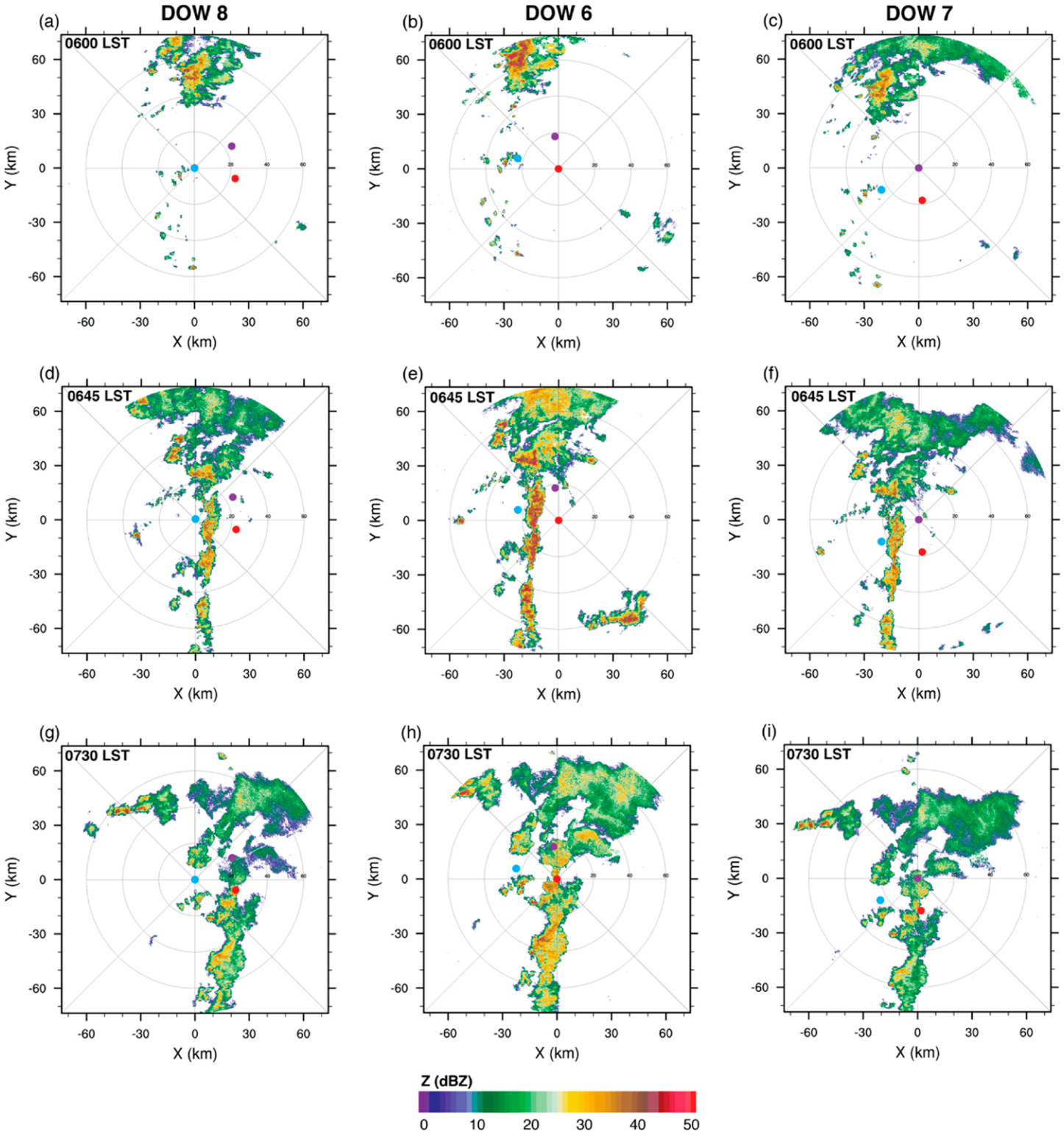

Fig. 8. Radar reflectivity (*Z*) at 1.2° elevation from (left) DOW8, (center) DOW6, and (right) DOW7 radar at (a)–(c) 0600, (d)–(f) 0645, and (g)–(i) 0730 LST 23 Jul 2018. The locations of the radars are shown with a blue dot (DOW8), red dot (DOW6), and purple dot (DOW7). North is located toward the top of the figure. For clarity, radar reflectivity below 2 dB*Z* is not plotted.

observed in the wind profilers signal-to-noise ratio at each site (Figs. 10e,f), until reaching a maximum height in the early afternoon (i.e., just after noon local time). Note that the white and black curves in the figures showing the PBLH as determined by the bulk Richardson number (Vogelezang and Holtslag 1996; Seidel et al. 2012) and the lifting condensation level (LCL; Bolton 1980), respectively. Given the larger sensible heat fluxes over nonirrigated cropland,

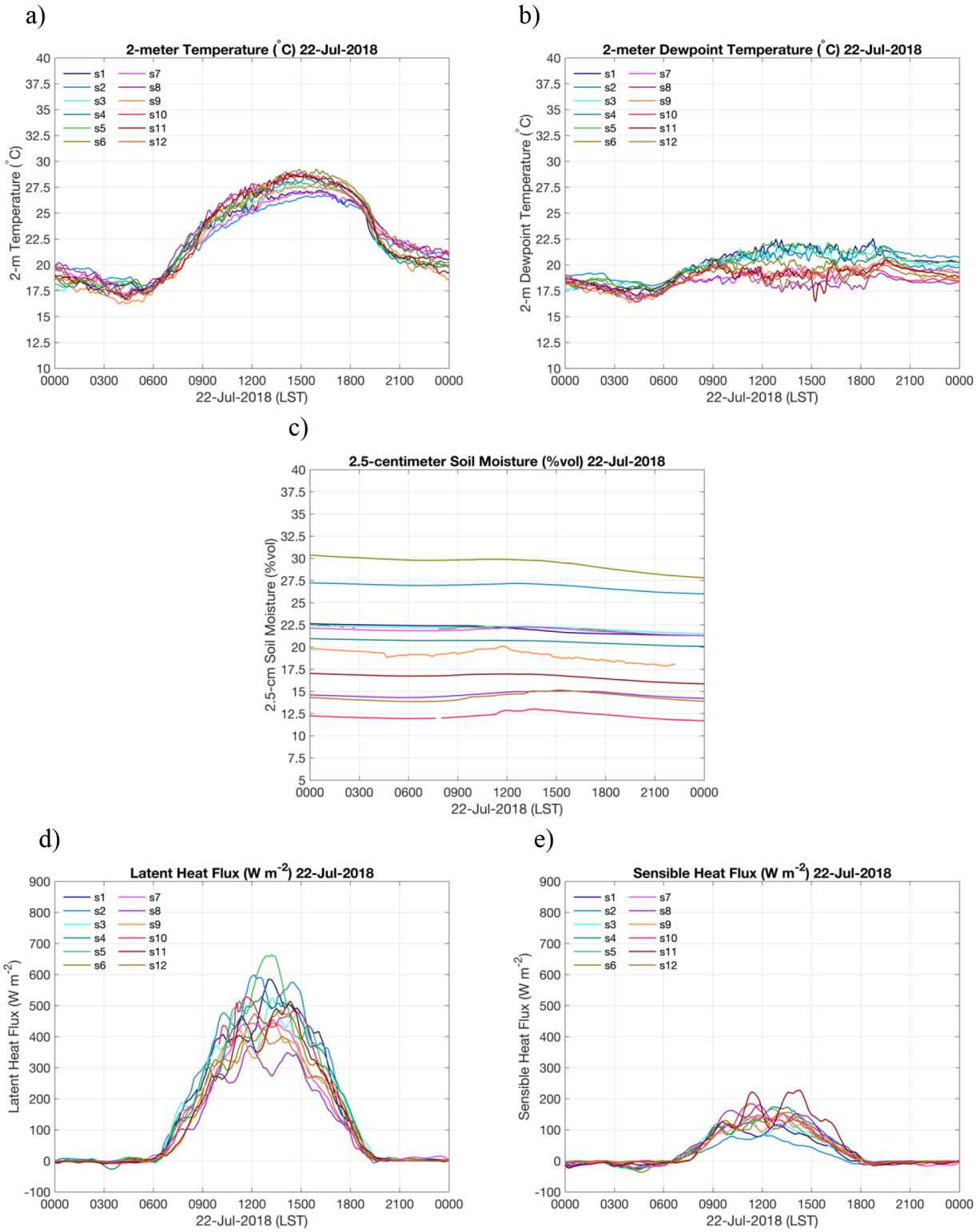

Fig. 9. ISFS site data on 22 Jul 2018 for (a) 2-m temperature, (b) 2-m dew point temperature, (c) soil moisture, (d) latent heat flux, and (e) sensible heat flux over irrigated [sites 1–6 (shown as s1–s6 with bluish colors)] and nonirrigated [sites 7–12 (shown as s7–s12 with reddish colors)] ISFS sites.

the maximum boundary layer height attained a higher altitude, just over 1 km AGL, compared to PBLH over irrigation, which grew to around 850 m.

The soundings for 22 July reveal a stronger stable surface layer at the Rogers Farm ISS site compared to that of the York site (supplementary Figs. ES3a–d). In terms of PBLH, the peak height occurred at the 1300 LST sounding in York while the maximum in Rogers Farm occurred at the 1500 LST sounding, again indicative of the larger sensible heating over the

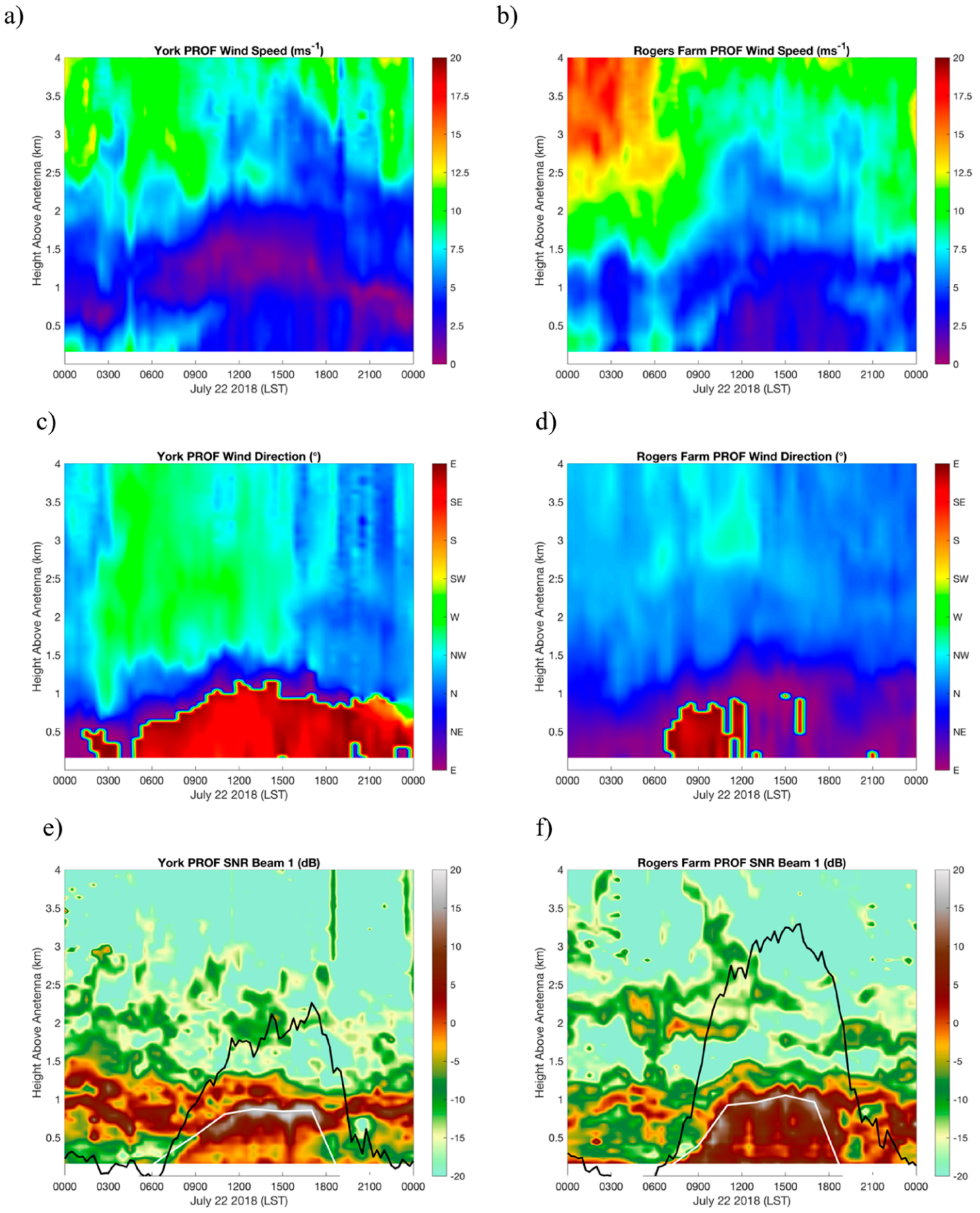

Fig. 10. 915-MHz wind profiler plots for (left) York and (right) Rogers Farm ISS sites for 22 Jul 2018: (a),(b) wind speed, (c),(d) wind direction, (e),(f) signal-to-noise ratio (SNR) with boundary layer height calculated from sounding using critical Richardson number (white line) and lifting condensation level (LCL; black line), and (g),(h) skew *T*–log*p* from radiosondes from the first sounding of the morning (~1100 UTC, ~0500 LST).

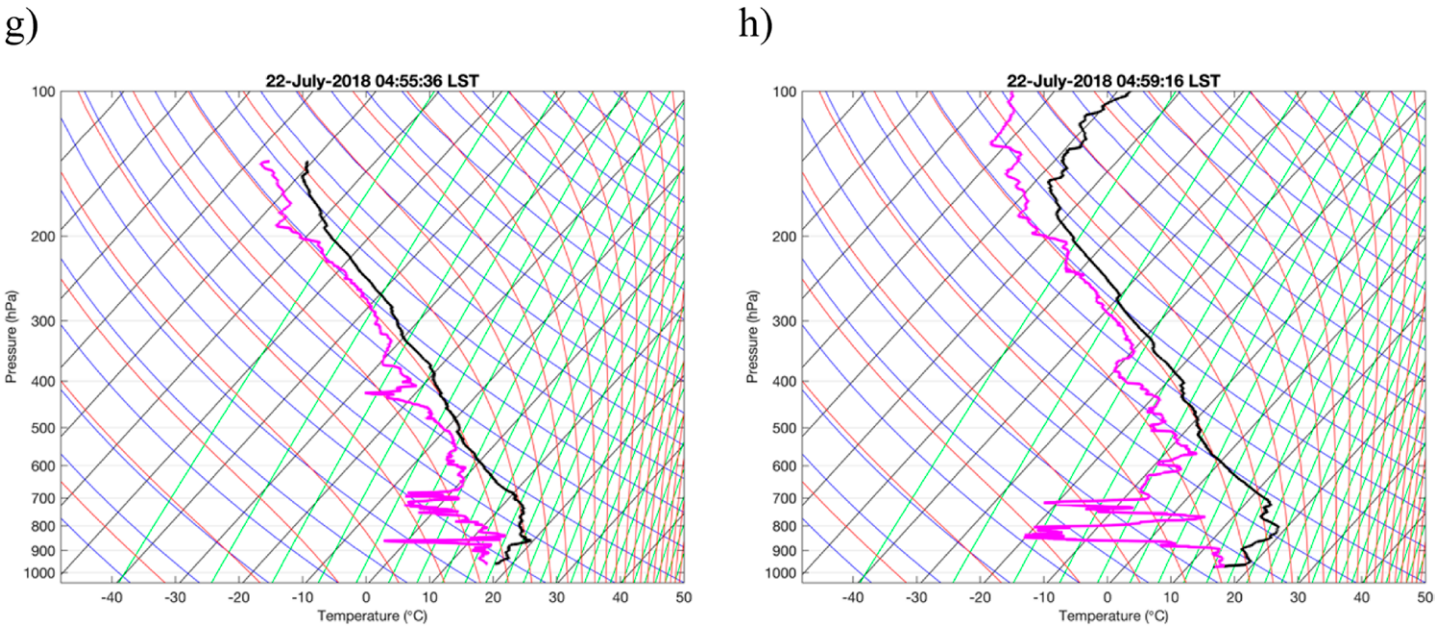

Fig. 10. Continued.

nonirrigated region. However, the weak surface inversion at York permitted its more rapid growth compared to the strong surface stratification prior to sunrise at Rogers Farm. It is also evident from the soundings that there was a capping inversion over York. Therefore, the lower PBLH at York can be contributed to both weaker sensible heat fluxes and a stronger capping inversion. Finally, the presunrise skew T–log$p$ plots (Figs. 10g,h) show the moister boundary layer over irrigation with a much shallower dry layer limited to the region of sharp direction wind shear in the entrainment layer. Over Rogers Farm, the entrainment layer was much thicker extending from 1 to 2 km AGL. Note that the entrainment was maximum after the morning transition, bringing drier air from above the inversion into the PBL and surface layer which increased evaporative demand from the irrigated and nonirrigated vegetation.

Much different conditions presented themselves on 23 July as the surface front moved into the GRAINEX study area (Figs. 7a,b). Similarity of air and dewpoint temperatures at irrigated sites suggests that air was saturated at 2 m roughly from 0000 to 0800 LST 23 July while the nonirrigated sites were close to saturation from 0400 to 0800 LST 23 July (supplementary Figs. ES4a,b). The overcast conditions also led to decreased surface fluxes on 23 July (supplementary Figs. ES4c,d). However, rain fell over irrigated sites (discussed below) in the morning hours so the sensible heat fluxes were constrained. The front passed through the entire GRAINEX region by around 1400 LST 23 July, leaving behind mostly sunny skies prior to the afternoon to evening transition. As a result, a stable boundary layer developed across the entire region as evidenced by the negative sensible heat fluxes across all sites.

An increase (decrease) in dewpoint was observed over irrigated (nonirrigated) sites between 0600 and 1400 LST (1200 and 1600 LST, although there was a slight increase as the sun rose and latent heating commenced), a result of PBL entrainment from above and the continued physical evaporation and transpiration. Advection is assumed to be small, given boundary layer winds that are generally calm and rarely exceed 5 m s^{-1}. Weak large-scale advection may also suggest why the air and dewpoint temperature at 2 m largely followed the diurnal surface flux evolution. The winds increased from the north after 1500 LST 23 July over irrigated (not shown) and after 1800 LST 23 July over nonirrigated (not shown) areas which caused the dewpoints to decline rapidly over both land uses (supplementary Figs. ES4a,b).

As discussed in the synoptic evolution, a convective line associated with a cold front extended from western Minnesota to just west of the GRAINEX area with a southwest–northeast

orientation at around 0300 LST 23 July. While the precipitation was broken up west of the GRAINEX area, it maintained intensity on the north side of the domain. Subsequently, as the cold front propagated east-southeast across the northern portion of the GRAINEX region, a line developed east of Rogers Farm. Around 0600 LST a meridional convective line developed directly over DOW8 (Figs. 8a–c), moved eastward and intensified as it approached DOW6 and DOW7 (Figs. 8d–f), and stalled and decayed over and eastward of DOW6 and DOW7 around 0730 LST (Figs. 8g–i).

The most unstable convective available potential energy (MUCAPE) is shown in Figs. 11a–c and is calculated using a reversible moist adiabat with ice. The use of MUCAPE to characterize buoyancy mitigates inaccuracies that early morning inversions can have on surface-based CAPE calculations. By the late morning, however, standard surface-based CAPE and MUCAPE are typically equivalent. On 22 July (Fig. 11a), MUCAPE is relatively small and constant throughout the sounding period of the day. It is worth noting that MUCAPE over the irrigated York ISS site is consistently larger (blue curve) than that of the nonirrigated Rogers Farm ISS site (red curve). On 23 July (Fig. 11b), MUCAPE was suppressed during the precipitation event at 1300 LST but quickly rebounded due to the near-saturated conditions that exist throughout the day in the lower troposphere. The MUCAPE increased rapidly in the western, irrigated sites (DOW8, ISS-York) followed by the other two DOW sites that straddle the irrigation gradient (DOW6 and DOW7) and at the nonirrigated ISS–Rogers Farm site. Unsurprisingly, MUCAPE declined to low values on 24 July (Fig. 11c).

One of the best examples of local L-A interactions during IOP2 was on 24 July (Figs. 12a–f). High pressure had settled in over the GRAINEX study area (Figs. 7e–f) with clearing during overnight hours leading to rapid temperature decline (Fig. 12a). In addition, a faster temperature decline occurred over irrigated sites as the dewpoint temperature (Fig. 12b) had already begun to lower after the frontal passage late from 1800 to 2400 LST 23 July (first half of the local evening). During the second half of the local evening/early morning, 0000 to 0600 LST 23 July, the irrigated sites cooled to the dewpoint and dew formed. Several nonirrigated cropland sites do not quite reach saturation during the overnight cooling period. During the first 6 h after sunrise, from 0600 to 1200 LST, there was a rapid increase in 2-m temperature (Fig. 12a), and a decrease in both PBL and lower-tropospheric wind speeds

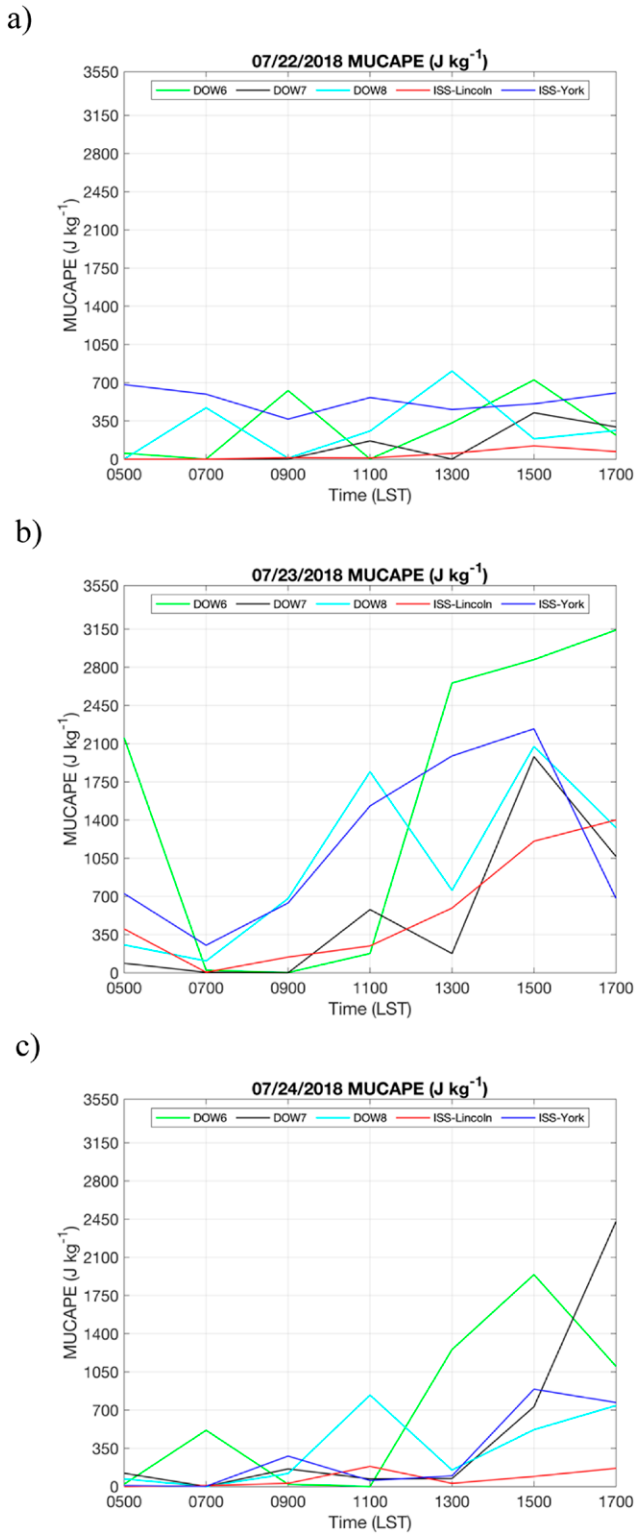

Fig. 11. MUCAPE calculated from daily soundings at the two ISS and three DOW sites for (a) 22, (b) 23, and (c) 24 Jul 2018.

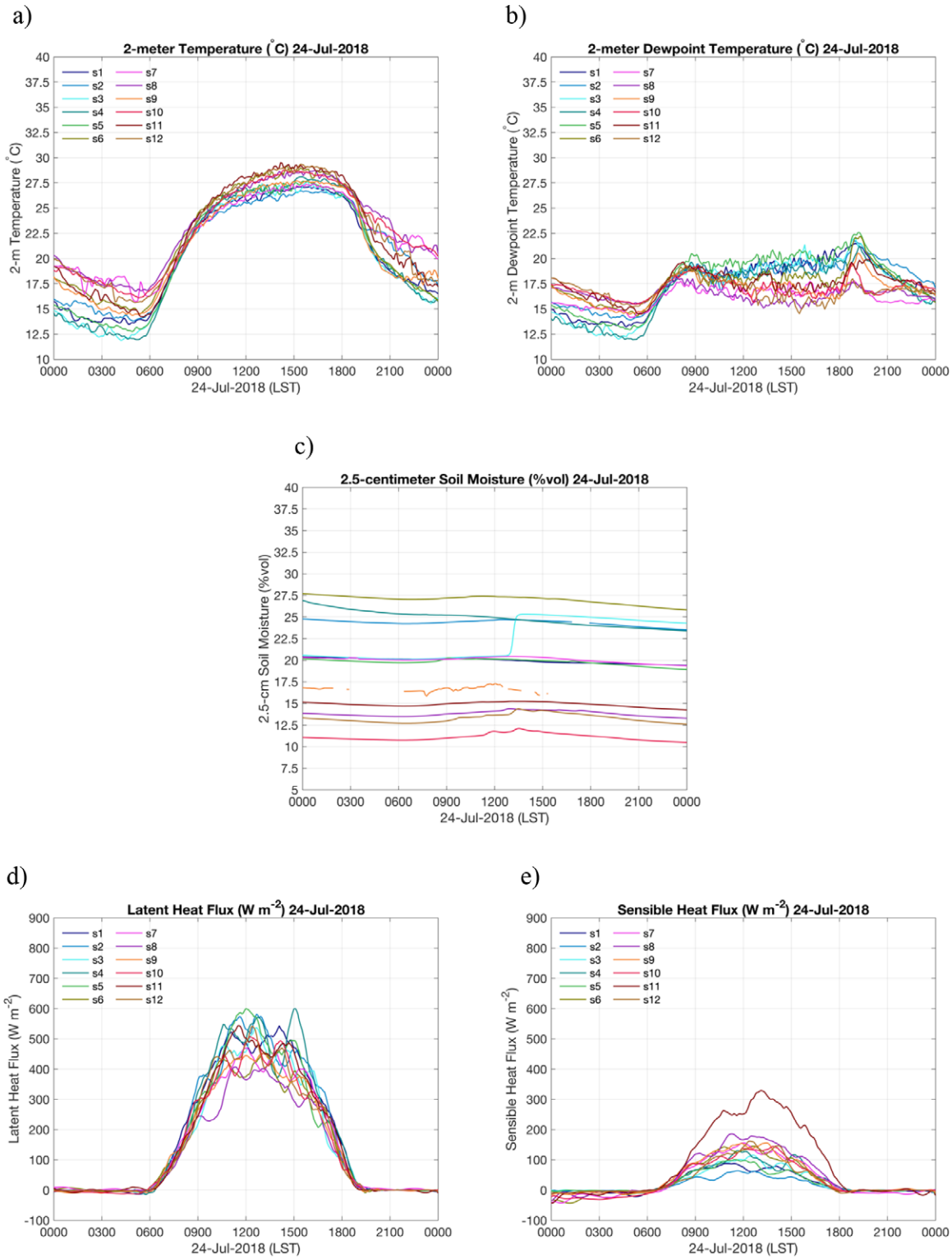

Fig. 12. As in Figs. 9a–e, but for 24 Jul 2018.

mostly in the north-northeasterly direction (Figs. 13a–d). The dewpoint temperature also increased with daybreak, likely due to the physical evaporation of dew. In addition, diverging of the 2-m temperature, humidity, and surface fluxes (Fig. 12) between irrigated and nonirrigated locations on 24 July provides a clear example of the role of irrigation on near-surface meteorology.

The PBL grew rapidly and was well mixed over both ISS sites by 1100 LST as can be found in both the signal-to-noise ratio (Figs. 13e,f) and radiosondes (Figs. 14a–f). The LCL at both sites (black curves in Figs. 13e,f) increased rapidly after sunrise, well before the PBL mixed

layer developed, to 3 km over irrigated and above 4 km on nonirrigated croplands, after which little variation was observed until the after-evening transition. The morning sounding over irrigated York shows a classic nocturnal boundary layer structure with a strong inversion (nearly 10°C in the lowest 250 m) underlying a weakly stable layer that extends up to 1.25 km. In contrast, over nonirrigated Rogers Farm the layer overlying the strong inversion was neutral. Further inspection of data suggests that vertical shear existed between 500

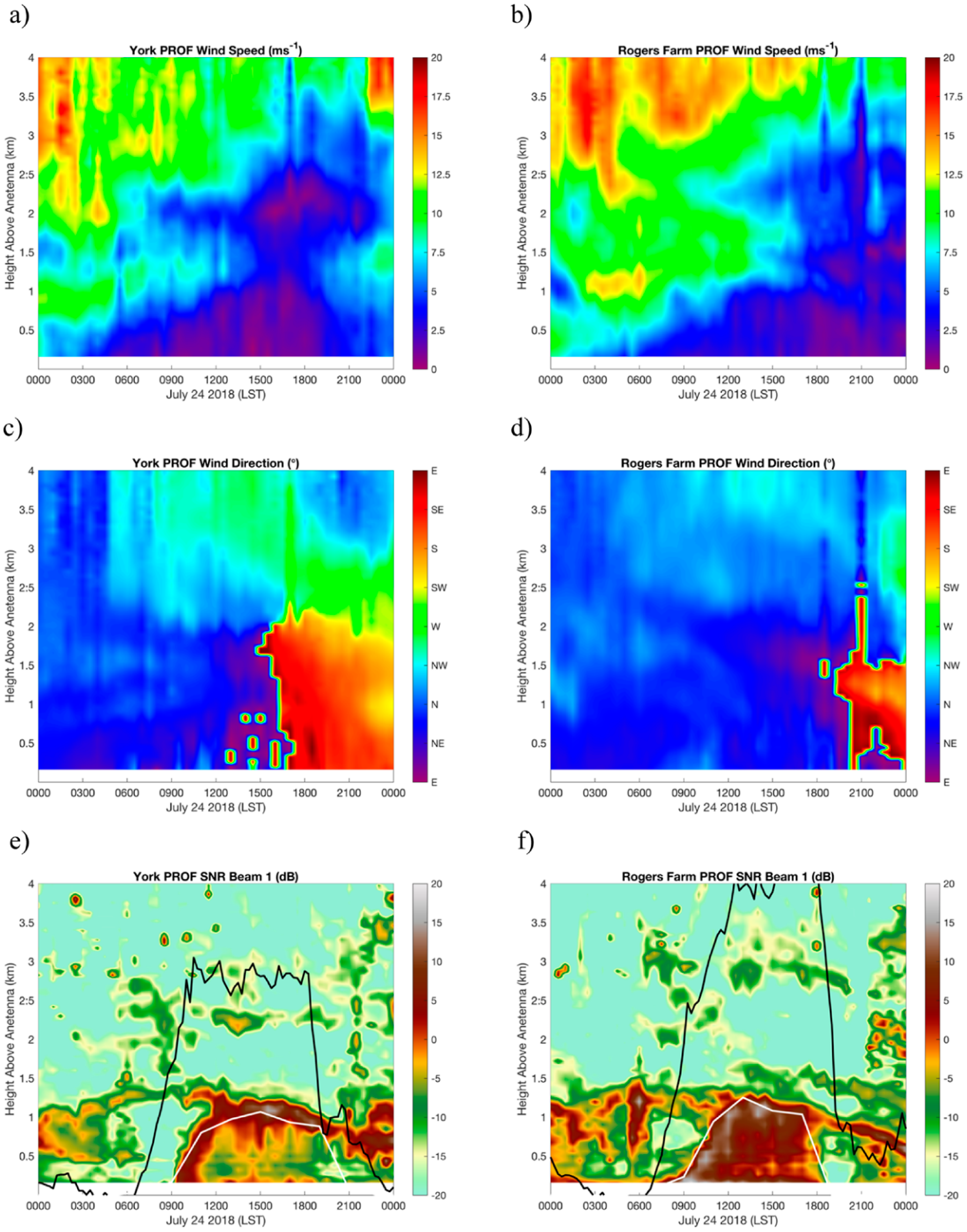

Fig. 13. As in Figs. 10a–f, but for 24 Jul 2018.

and 1,000 m at both locations from 0100 to 0700 LST (Figs. 13 a,b). The shear was stronger over nonirrigated Rogers Farm so that shear production and breaking waves may force this layer toward neutral stratification compared to the weakly stable conditions over York. The absence of vertical turbulence profiles prohibited further investigation and verifying this suggestion. There was a slightly stronger capping inversion over irrigated York as observed

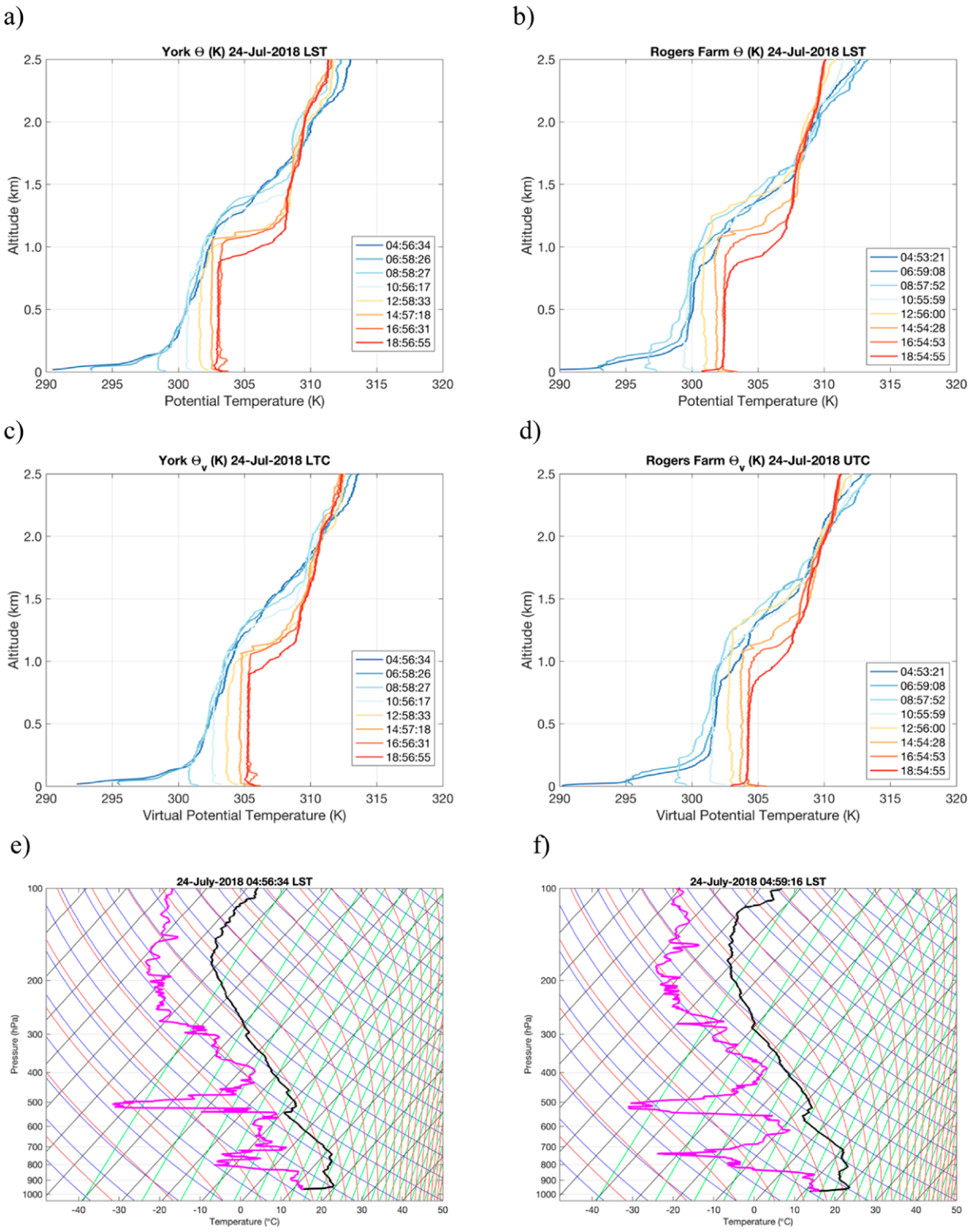

Fig. 14. Radiosonde profiles on 24 Jul 2018 from the (left) York and (right) Rogers Farm ISS sites eight times daily from ~0500 LST to ~1900 LST: (a),(b) boundary layer and lower-free-atmosphere θ, (c),(d) boundary layer and lower-free-atmosphere θ_v, and (e),(f) air temperature and dewpoint temperature through the troposphere.

in the potential temperature and virtual temperature soundings (Figs. 14a–d) while PBL top entrainment was stronger over the nonirrigated ISS site in Rogers Farm as indicated by the higher PBLH. In the afternoon, observed PBLH has stabilized over irrigated York at just above 1 km. On the other hand, the PBLH decreased over nonirrigated Rogers Farm by late afternoon to a value similar to that over York by 1700 LST. Although it is more pronounced over the Rogers Farm, the PBLH decreased over both locations by sunset.

Diagnosing PBL evolution with mixing diagrams. The ISS-York (in close proximity to ISFS site 2) and the ISS–Rogers Farm (in close proximity to ISFS site 9) (Fig. 1) is used to approximate land surface states, near-surface meteorology, and atmospheric profile data in order to produce mixing diagrams (Figs. 15a–f). Mixing diagrams were introduced by Betts (1984, 1992). They were further highlighted by Santanello et al. (2009, 2011, 2018) as a tool for diagnosing local land–atmosphere interactions. Mixing diagrams are a vector approach to describing the diurnal growth and decay of the convective boundary layer from a heat and moisture budget perspective. The methodology employs a boundary layer moist static energy (MSE) column budget approach for the understanding of L-A interactions by considering fluxes through the bottom boundary (surface fluxes), lateral boundaries (advection), and top boundary (entrainment). For the analysis carried out here, only surface fluxes were utilized with entrainment calculated as a residual as described in the documentation for L-A interactions metrics produced for GEWEX/Global Land/Atmosphere System Study (GLASS) (http://cola.gmu.edu/dirmeyer/Coupling_metrics.html). Small magnitude processes, such as advection and nonadiabatic terms are contained as part of the entrainment term.

Four quantities that are difficult to observe but can be obtained from mixing diagrams (Santanello et al. 2009, 2011) are 1) the surface Bowen ratio ($\beta_s = \mathrm{SH}_s/\mathrm{LH}_s$), 2) the entrainment Bowen ratio ($\beta_e = \mathrm{SH}_e/\mathrm{LH}_e$), 3) the latent heat entrainment ratio ($A_l = \mathrm{LH}_e/\mathrm{LH}_s$), and 4) the sensible heat entrainment ratio ($A_h = \mathrm{SH}_e/\mathrm{SH}_s$). In these four quantities, subscripts *l*, *h*, *e*, and *s* represent latent heating, sensible heating, evaluation in the entrainment layer, and evaluation at the surface, respectively. Note that in Figs. 15a, 15c, and 15e, the dashed lines are vectors representing the surface and entrainment fluxes and yield the Bowen ratio of the surface and entrainment (Santanello et al. 2009). The values of the quantities for each of the days considered is shown in Table 5, where the daily mean values are given. Two-hourly values were also calculated, corresponding to the sounding time interval, which resulted in similar values to that of the daily mean when aggregated, as was observed in Santanello et al. (2009).

On 22 July, the morning hours were dominated by warming and moistening at both locations (Fig. 15a), resulting in decreasing relative humidity but increasing equivalent potential temperature (Fig. 15b). Close to noon (1100 LST), the PBLH had attained its largest value capping a well-mixed boundary layer. The larger PBLH over Rogers Farm suggests a greater entrainment of warm, dry air from the free troposphere resulting in warming, and slight drying of the 2-m air as can be observed in the mixing diagram (Fig. 15a), leading to a near-constant θ_e and declining relative humidity (Fig. 15b). There was minimal drying at 2 m over York and while the humidity went down (rapidly in the morning, then slowly in the afternoon), θ_e increased throughout the day. In other words, at midday solar heating dominated the surface Bowen ratio evolution with entrainment drying dominating the Rogers Farm signature while surface moistening from physical evaporation at York resulted in the maintenance of a positive slope to the surface Bowen ratio. Prior to sunset (the darkest dots in Figs. 15a,b) there was a period of moistening leading to a rise in relative humidity at both sites. This period of moistening and slow cooling is associated with increased moisture flux convergence during the afternoon–evening transition. One point worth considering is that southeastern Nebraska experiences a humid continental climate, not semiarid where L-A interactions is significantly

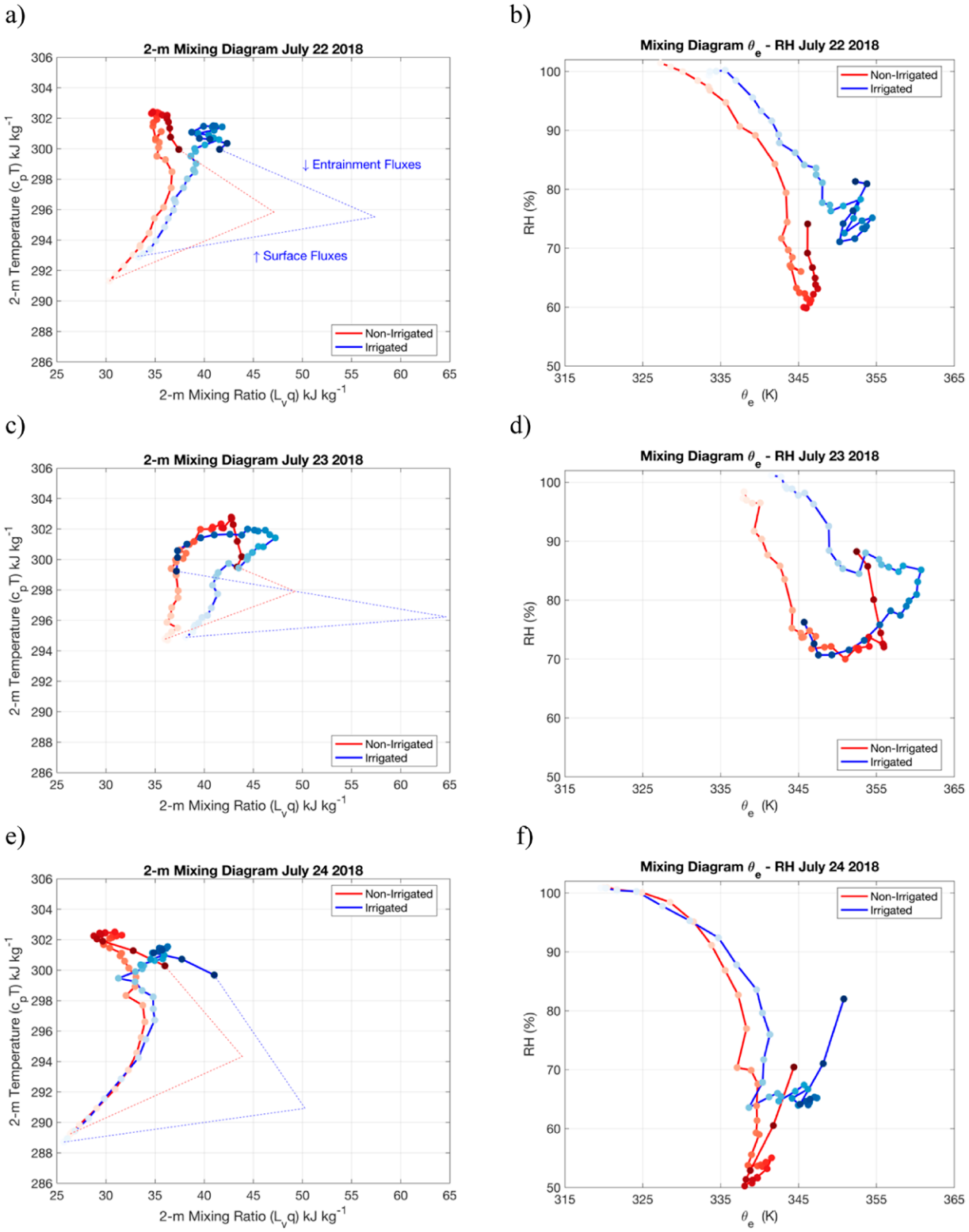

Fig. 15. Mixing diagrams, or the temporal evolution of the moisture and heat terms of the (left) surface moist static energy and (right) relative humidity–θ_e space for (a),(b) 22, (c),(d) 23, and (e),(f) 24 Jul 2018. The temporal evolution is from sunrise to sunset with each segment lasting 20 min and the dots getting darker as the day gets longer. Dotted lines in (a), (c), and (e) show the Bowen ratio slope of the surface (lower) and entrainment (upper) for irrigated (blue) and nonirrigated (red) cropland.

more pronounced. Furthermore, spring and summer of 2018 were wet and there were clear differences between soil moisture over irrigated and nonirrigated croplands as reflected in the ISFS soil moisture plots (Figs. 9c and 12c).

The daily mean surface (entrainment) Bowen ratio has a value nearly 3 (1.5) times larger over nonirrigated cropland compared to irrigated cropland. It is suggestive of the larger magnitude of sensible heating and smaller magnitude of latent heat fluxes over nonirrigated areas (Figs. 15a,b). The surface Bowen ratio was maximized in the morning and decreased throughout the day (not shown) as both latent and sensible heat fluxes were increased with relative magnitudes being larger at both locations. This is, again, indicative of the most rapid boundary layer growth occurring between sunrise and noon local time. At noon local time, the surface Bowen ratio difference between irrigated and nonirrigated cropland was maximized where it was 3 times larger over nonirrigated areas compared to the irrigated. The entrainment-layer Bowen ratio was similar to that of the surface, although it was typically negative given that warm (positive heat flux) and dry air (negative moisture flux) entrained into the boundary layer from the free atmosphere. Again, the most negative values were found in the morning with increasing values throughout the day, turning positive just before and during the evening transition (not shown). The

Table 5. Mixing diagram Bowen and entrainment ratios (York/Lincoln).

	β_s (York/Lincoln)	β_e (York/Lincoln)	A_l (York/Lincoln)	A_h (York/Lincoln)
22 Jul 2018	0.11/0.27	−0.35/-0.57	−0.68/-0.65	2.2/1.4
23 Jul 2018	0.05/0.24	−0.22/-0.75	−0.48/-0.92	3.93/1.54
24 Jul 2018	0.09/0.29	−0.70/-0.55	−0.61/-0.84	4.75/1.58

entrainment ratios are much more similar in magnitude (Table 5) in terms of the daily aggregate, with the moisture entrainment flux being significantly larger over irrigated land uses due to the overall weaker entrainment coupled with a larger surface moisture flux. The same can be said for the nonirrigated areas, where the heat fluxes at both the surface and the entrainment layer are maximized in late morning and decreased proportionally through the afternoon.

On 23 July, the frontal passage, as discussed in the synoptic evolution, led to a much different mixing diagram than the previous day (Figs. 15c,d). Due to cloud cover inhibiting longwave radiative cooling, surface air temperatures remained high overnight. Also, the moisture term in moist static energy at sunrise was the same as at sunset of the previous night at Rogers Farm but has decreased slightly at York. The 2-m temperature increased at both sites during the morning hours, but the 2-m humidity remains near constant at Rogers Farm, resulting in a decreasing relative humidity and a near-constant θ_e (Figs. 15c,d). At ISS-York, the near-surface moisture increased rapidly in the morning as the squall line developed between the York site and the Big Blue River. The mixing ratio began to fall rapidly well before the temperature started to decrease, providing further support of a frontal passage prior to sunset. In contrast, the ISS-Lincoln site underwent moistening until a few hours before sunset at which point the temperature began to fall, moistening weakened, and drying commenced with frontal passage at the final observation time (1900 LST 24 July 2018). As a result, both relative humidity and θ_e decreased with time in the afternoon at York. On the other hand, relative humidity decreased and θ_e increased with time at Rogers Farm until just prior to sunset. In terms of daily aggregates, the surface Bowen ratio at Rogers Farm was 5 times larger than that at York while the entrainment layer Bowen ratio magnitude at York was 3 times that at Rogers Farm. The surface Bowen ratio can be explained with the aid of supplementary Figs. ES4c and 4d where the latent heat flux was about 25% larger over irrigated cropland compared to nonirrigated. The smaller magnitude of latent heat flux over Rogers Farm was therefore responsible for the consistently larger surface Bowen ratio.

Unlike 22 July, the entrainment ratios were quite different at the two sites. The entrainment layer Bowen ratio and entrainment heat and moisture fluxes must be carefully considered as the overcast moist day did not provide ideal conditions for L-A observations as observed in the soundings (not shown). As noted above, advective tendencies in the moist static energy budget are difficult to assess in an observational study and will be addressed in a forthcoming modeling study.

On 24 July, conditions were similar to 22 July with high surface pressure and cloud-free skies. The strong cooling and drying after the frontal passage led to the lowest values observed in moist static energy at sunrise. The latent and sensible heat components of moist static energy increased in a similar manner during the morning hours (Figs. 15e,f) until the mixed layer had grown to near the PBLH and entrainment is effective at modifying the surface temperature and humidity. With the temperature and moisture increasing, θ_e increased slightly as the relative humidity plummeted. During the afternoon, dry air originating out of the north entrained into the PBL from the free atmosphere. As discussed previously, the ISS–Rogers Farm site observed drier air capping the inversion as the winds at York became westerly on 24 July in advance of another precipitation system that arrived on 25 July (not shown). As a result, and in contrast to the two previous days, the entrainment layer Bowen ratio has a larger magnitude over York than over Rogers Farm and the moisture term of moist static energy over York was lower than that of Rogers Farm.

Conclusions

The Great Plains Irrigation Experiment (GRAINEX) was conducted in the spring and summer of 2018 to investigate the role of the onset and continued widespread application of irrigation on PBL evolution and near-surface meteorology in southeastern Nebraska which includes adjacent irrigated and nonirrigated areas. GRAINEX is the first of this type of field campaign that has solely focused on the impacts of irrigated versus nonirrigated land uses on the atmosphere. This study is particularly important and timely in the context of rapid expansion of irrigated agriculture globally and its potential impacts on weather and climate. This paper presented initial results of analysis of data from GRAINEX.

The study finds that early in the growing season (IOP1), differences in temperatures between irrigated and nonirrigated regions were relatively small compared to the middle of the growing season (IOP2) with cooler temperatures over irrigated areas during both time periods. The observed mixing ratio also showed similar patterns with higher mixing ratios over irrigated land. Generally, the daily differences between latent and sensible heat fluxes were also smaller during the early growing season over both irrigated and nonirrigated land while they were larger during the peak growing season over irrigated areas. Consistent with these findings, higher soil moisture and lower turbulent kinetic energy was reported during the peak growing season and planetary boundary height was lower over irrigated land (Fig. 16).

Observations also demonstrate the influence of irrigation on the daily evolution of these variables as well as MUCAPE, Bowen ratio, equivalent potential temperature, planetary boundary layer height, and several other land–atmosphere interaction measures. In addition, initial assessment suggests that irrigated land use may have influenced precipitation events over the study area. Future studies will include additional assessment of the observed data from the GRAINEX and numerical modeling to further understand the process and mechanisms via which irrigated and nonirrigated land use impacts lower troposphere and weather.

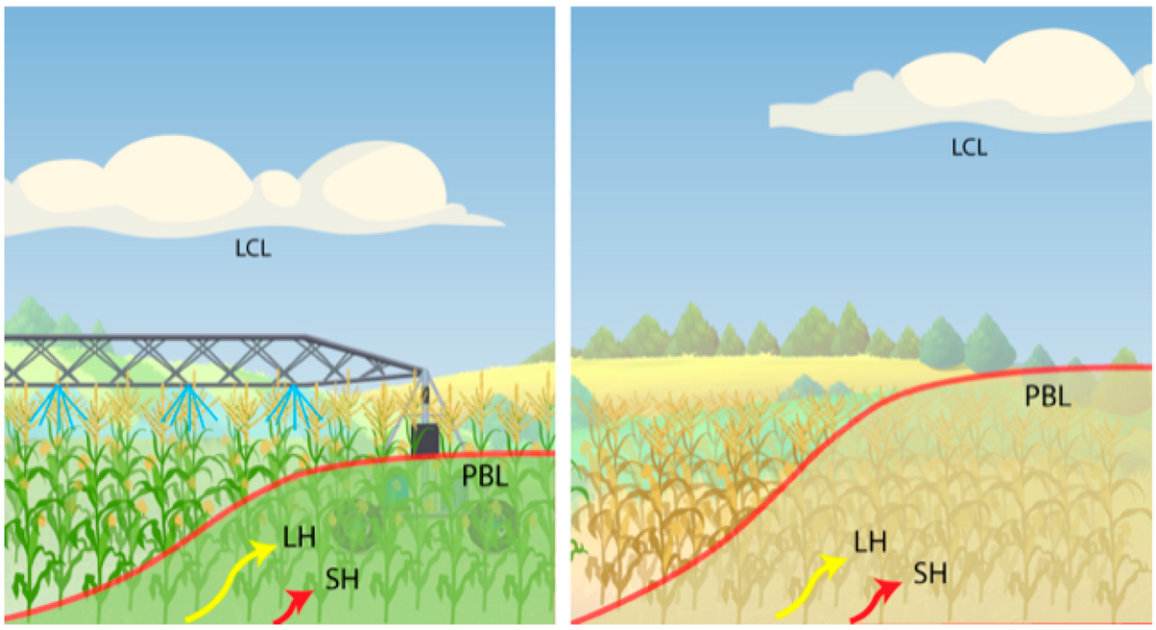

Fig. 16. A conceptual diagram of changes in lifting condensation level (LCL), planetary boundary layer (PBL), latent heat flux (LH), and sensible heat flux (SH) over (a) irrigated and (b) nonirrigated land use–land cover. In (a), due to irrigation, latent heat flux is greater and sensible heat flux is less. On the other hand, over nonirrigated land use in (b), LH is greater compared to SH but the difference between the two (LH vs SH) is much less. Overall, SH is greater over nonirrigated land compared to irrigated land. This condition also impacts depth of the PBL and results in higher PBL height over nonirrigated land. Relatively higher LH and moistness over irrigated land resulted in lower LCL compared to nonirrigated land.

Acknowledgments. The authors thank three anonymous reviewers for their valuable comments and suggestions, which helped to improve this paper. This research is funded by the NSF Grants AGS-1853390 (Rezaul Mahmood and Eric Rappin), AGS-1720477 (Udaysankar Nair), and AGS-1552487 (Roger Pielke). Thanks to team members from the NCAR/Lower Atmosphere Observation Facilities and the Center for Severe Weather Research for operating ISS, ISFS, and DOW observation platforms. The NASA Science Utilization of SMAP program (PM: Jared Entin) supported GREX deployment and the participation of Joseph Santanello, Edward Kim, and Patricia Lawston-Parker. Thanks go to additional NASA personnel Albert Wu, Rajat Bindlish, pilots and support staff for the Twin Otter where GREX was mounted, and NASA-affiliated students. Feedback provided during project development by Kevin Knupp and Paul Dirmeyer is gratefully acknowledged. The PIs of the project are also grateful to Nebraska Extension personnel, including, Randy Pryor, Aaron Nygren, Gary Lesoing, Tyler Williams, Brandy VandeWalle, and Jenny Reese; Nebraska's Natural Resources Districts personnel Dick Ehrman, Chuck Wingert, Tyler Benal, Rod DeBuhr, and Daryl Anderson; and Al Dutcher and Stonie Cooper of the Nebraska State Climate Office. Together they played a key role in site selection and connecting PIs to nearly 100 landowners. Access to land for siting observation platforms was critical to success of the GRAINEX project and the PIs are thankful for the generosity of the landowners. Thanks also to Adam Houston for recruiting students from the Department of Earth and Atmospheric Science, University of Nebraska–Lincoln (UNL), who assisted in the field work. Similarly, thanks go to students from the School of Natural Resources, UNL, and the Meteorology Program, Department of Geography and Geology, Western Kentucky University. Thanks to Dallas Staley for her excellent technical editing.

References

Adegoke, J. O., R. A. Pielke Sr., J. Eastman, R. Mahmood, and K. G. Hubbard, 2003: Impact of irrigation of midsummer surface fluxes and temperature under dry synoptic conditions: A regional atmospheric model study of the U.S. High Plains. *Mon. Wea. Rev.*, **131**, 556–564, https://doi.org/10.1175/1520-0493(2003)131<0556:IOIOMS>2.0.CO;2.

Archer, C. L., and K. Caldeira, 2008: Historical trends in the jet streams. *Geophys. Res. Lett.*, **35**, L08803, https://doi.org/10.1029/2008GL033614.

Barnston, A., and P. T. Schickedanz, 1984: The effect of irrigation on warm season precipitation in the southern Great Plains. *J. Climate Appl. Meteor.*, **23**, 865–888, https://doi.org/10.1175/1520-0450(1984)023<0865:TEOIOW>2.0.CO;2.

Betts, A. K., 1984: Boundary layer thermodynamics of a High Plains severe storm. *Mon. Wea. Rev.*, **112**, 2199–2211, https://doi.org/10.1175/1520-0493(1984)112<2199:BLTOAH>2.0.CO;2.

——, 1992: FIFE atmospheric boundary layer budget methods. *J. Geophys. Res.*, **97**, 18 523–18 531.

Bolton, D., 1980: The computation of equivalent potential temperature. *Mon. Wea. Rev.*, **108**, 1046–1053, https://doi.org/10.1175/1520-0493(1980)108<1046:TCOEPT>2.0.CO;2.

Brovkin, V., and Coauthors, 2013: Effect of anthropogenic land-use and land-cover changes on climate and land carbon storage in CMIP5 projections for the twenty-first century. *J. Climate*, **26**, 6859–6881, https://doi.org/10.1175/JCLI-D-12-00623.1.

Campra, P., M. Garcia, Y. Canton, and A. Palacios-Orueta, 2008: Surface temperature cooling trends and negative radiative forcing due to land use change toward greenhouse farming in southeastern Spain. *J. Geophys. Res.*, **113**, D18109, https://doi.org/10.1029/2008JD009912.

Chen, C. J., C. C. Chen, M. H. Lo, J. Y. Juang, and C. M. Chang, 2020: Central Taiwan's hydroclimate in response to land use/cover change. *Environ. Res. Lett.*, **15**, 034015, https://doi.org/10.1088/1748-9326/ab68aa.

Costa, M. H., S. N. M. Yanagi, P. J. O. P. Souza, A. Ribeiro, and E. J. P. Rocha, 2007: Climate change in Amazonia caused by soybean cropland expansion, as compared to caused by pastureland expansion. *Geophys. Res. Lett.*, **34**, L07706, https://doi.org/10.1029/2007GL029271.

Davin, E. L., and N. de Noblet-Ducoudré, 2010: Climatic impact of global-scale deforestation: Radiative versus nonradiative processes. *J. Climate*, **23**, 97–112, https://doi.org/10.1175/2009JCLI3102.1.

DeAngelis, A., F. Dominguez, Y. Fan, A. Robock, M. D. Kustu, and D. Robinson, 2010: Evidence of enhanced precipitation due to irrigation over the Great Plains of the United States. *J. Geophys. Res.*, **115**, D15115, https://doi.org/10.1029/2010JD013892.

Devanand, A., M. Huang, M. Ashfaq, B. Barik, and S. Ghosh, 2019: Choice of irrigation water management practice affects Indian summer monsoon rainfall and its extremes. *Geophys. Res. Lett.*, **46**, 9126–9135, https://doi.org/10.1029/2019GL083875.

Gerken, T., B. L. Ruddell, R. Yu, P. C. Stoy, and D. T. Drewry, 2019: Robust observations of land-to-atmosphere feedbacks using the information flows of FLUXNET. *Climate Atmos. Sci.*, **2**, 37, https://doi.org/10.1038/s41612-019-0094-4.

Gero, A. F., A. J. Pitman, G. T. Narisma, C. Jacobson, and R. A. Pielke, 2006: The impact of land cover change on storms in the Sydney Basin, Australia. *Global Planet. Change*, **54**, 57–78, https://doi.org/10.1016/j.gloplacha.2006.05.003.

He, Y., E. Lee, and J. S. Mankin, 2020: Seasonal tropospheric cooling in northeast China associated with cropland expansion. *Environ. Res. Lett.*, **15**, 034032, https://doi.org/10.1088/1748-9326/ab6616.

Koster, R. D., and Coauthors, 2004: Regions of strong coupling between soil moisture and precipitation. *Science*, **305**, 1138–1140, https://doi.org/10.1126/science.1100217.

Kustas, W. P., J. L. Hatfield, and J. H. Prueger, 2005: The Soil Moisture–Atmosphere Coupling Experiment (SMACEX): Background, hydrometeorological conditions, and preliminary findings. *J. Hydrometeor.*, **6**, 791–804, https://doi.org/10.1175/JHM456.1.

Lawston, P. M., J. A. Santanello Jr., B. F. Zaitchik, and M. Rodell, 2015: Impact of irrigation methods on land surface model spinup and initialization of WRF forecasts. *J. Hydrometeor.*, **16**, 1135–1154, https://doi.org/10.1175/JHM-D-14-0203.1.

——, ——, T. E. Franz, and M. Rodell, 2017: Assessment of irrigation physics in a land surface modeling framework using non-traditional and human-practice datasets. *Hydrol. Earth Syst. Sci.*, **21**, 2953–2966, https://doi.org/10.5194/hess-21-2953-2017.

——, ——, B. Hanson, and K. Arsensault, 2020: Impacts of irrigation on summertime temperatures in the Pacific Northwest. *Earth Interact.*, **24**, https://doi.org/10.1175/EI-D-19-0015.1.

Mahmood, R., and K. G. Hubbard, 2002: Anthropogenic land-use change in the North American tall grass-short grass transition and modification of near-surface hydrologic cycle. *Climate Res.*, **21**, 83–90, https://doi.org/10.3354/cr021083.

——, ——, and C. Carlson, 2004: Modification of growing season surface temperature records in the northern Great Plains due to land use transformation: Verification of modeling results and implication for global climate change. *Int. J. Climatol.*, **24**, 311–327, https://doi.org/10.1002/joc.992.

——, ——, R. Leeper, and S. A. Foster, 2008: Increase in near-surface atmospheric moisture content due to land use changes: Evidence from the observed dew point temperature data. *Mon. Wea. Rev.*, **136**, 1554–1561, https://doi.org/10.1175/2007MWR2040.1.

——, and Coauthors, 2010: Impacts of land use/land cover change on climate and future research priorities. *Bull. Amer. Meteor. Soc.*, **91**, 37–46, https://doi.org/10.1175/2009BAMS2769.1.

——, and Coauthors, 2014: Land cover changes and their biogeophysical effects on climate. *Int. J. Climatol.*, **34**, 929–953, https://doi.org/10.1002/joc.3736.

Meehl, G. A., R. Moss, K. E. Taylor, V. Eyring, R. J. Stouffer, S. Bony, and B. Stevens, 2014: Climate model intercomparison: Preparing for the next phase. *Eos, Trans. Amer. Geophys. Union*, **95**, 77–78, https://doi.org/10.1002/2014EO090001.

Melillo, J. M., T. Richmond, and G. W. Yohe, 2014: Climate Change Impacts in the United States: The Third National Climate Assessment. J. M. Melillo, T. C. Richmond, and G. W. Yohe, Eds., U.S. Global Change Research Program, 841 pp.

Miralles, D. G., W. Brutsaert, A. J. Dolman, and J. H. Gash, 2020: On the use of the term "evapotranspiration." *Water Resour. Res.*, **56**, e2020WR028055, https://doi.org/10.1029/2020WR028055.

Nikiel, C. A., and E. A. Eltahir, 2019: Summer climate change in the Midwest and Great Plains due to agricultural development during the twentieth century. *J. Climate*, **32**, 5583–5599, https://doi.org/10.1175/JCLI-D-19-0096.1.

NRC, 2005: *Radiative Forcing of Climate Change: Expanding the Concept and Addressing Uncertainties*. National Academies Press, 222 pp.

——, 2012: *Urban Meteorology: Forecasting, Monitoring, and Meeting Users' Needs.* National Academies Press, 190 pp.

Pielke, R. A., Sr., 2018: Daily weather discussions. Version 1.0. UCAR/NCAR Earth Observing Laboratory, accessed August 2019, https://data.eol.ucar.edu/dataset/561.010.

——, and Coauthors, 2011: Land use/land cover changes and climate: Modeling analysis and observational evidence. *Wiley Interdiscip. Rev.: Climate Change*, **2**, 828–850, https://doi.org/10.1002/wcc.144.

——, R. Mahmood, and C. McAlpine, 2016: Land's complex role in climate change. *Phys. Today*, **69**, 40–46, https://doi.org/10.1063/PT.3.3364.

Pitman, A. J., and Coauthors, 2009: Uncertainties in climate responses to past land cover change: First results from the LUCID intercomparison study. *Geophys. Res. Lett.*, **36**, L14814, https://doi.org/10.1029/2009GL039076.

Puma, M. J., and B. I. Cook, 2010: Effects of irrigation on global climate during the 20th century. *J. Geophys. Res.*, **115**, D16120, https://doi.org/10.1029/2010JD014122.

Santanello, J. A., C. D. Peters-Lidard, S. V. Kumar, C. Alonge, and W.-K. Tao, 2009: A modeling and observational framework for diagnosing local land–atmosphere coupling on diurnal time scales. *J. Hydrometeor.*, **10**, 577–599, https://doi.org/10.1175/2009JHM1066.1.

——, ——, and ——, 2011: Diagnosing the sensitivity of local land–atmosphere coupling via the soil moisture–boundary layer interaction. *J. Hydrometeor.*, **12**, 766–786, https://doi.org/10.1175/JHM-D-10-05014.1.

——, and Coauthors, 2018: Land–atmosphere interactions: The LoCo perspective. *Bull. Amer. Meteor. Soc.*, **99**, 1253–1272, https://doi.org/10.1175/BAMS-D-17-0001.1.

Segal, M., J. R. Garratt, R. A. Pielke, W. E. Schreiber, A. Rodi, G. Kallos, and J. Weaver, 1989: The impact of crop areas in northeast Colorado on midsummer mesoscale thermal circulations. *Mon. Wea. Rev.*, **117**, 809–825, https://doi.org/10.1175/1520-0493(1989)117<0809:TIOCAI>2.0.CO;2.

Seidel, D. J., Y. Zhang, A. Beljaars, J. C. Golaz, A. R. Jacobson, and B. Medeiros, 2012: Climatology of the planetary boundary layer over the continental United States and Europe. *J. Geophys. Res.*, **117**, D17106, https://doi.org/10.1029/2012JD018143.

Sen Roy, S., R. Mahmood, A. I. Quintanar, and A. Gonzalez, 2011: Impacts of irrigation on dry season precipitation in India. *Theor. Appl. Climatol.*, **104**, 193–207, https://doi.org/10.1007/s00704-010-0338-z.

Szilagyi, J., and T. E. Franz, 2020: Anthropogenic hydrometeorological changes at a regional scale: Observed irrigation–precipitation feedback (1979–2015) in Nebraska, USA. *Sustain. Water Resour. Manage.*, **6**, 1, https://doi.org/10.1007/s40899-020-00368-w.

Thiery, W., and Coauthors, 2020: Warming of hot extremes alleviated by expanding irrigation. *Nat. Commun.*, **11**, 290, https://doi.org/10.1038/s41467-019-14075-4.

UCAR/NCAR, 1990: NCAR Integrated Surface Flux System (ISFS), Earth Observing Laboratory, accessed 26 May 2021, https://doi.org/10.5065/D6ZC80XJ.

UCAR/NCAR, 1997: NCAR Integrated Sounding System (ISS), Earth Observing Laboratory, accessed 30 Mar 2021, https://doi.org/10.5065/D6348HF9.

Vogelezang, D. H. P., and A. A. M. Holtslag, 1996: Evaluation and model impacts of alternative boundary-layer height formulations. *Bound.-Layer Meteor.*, **81**, 245–269.

Weckwerth, T. M., and Coauthors, 2004: An overview of the International H_2O Project (IHOP_2002) and some preliminary highlights. *Bull. Amer. Meteor. Soc.*, **85**, 253–278, https://doi.org/10.1175/BAMS-85-2-253.

Wei, J., P. A. Dirmeyer, D. Wisser, M. C. Bosilovich, and D. M. Mocko, 2013: Where does the irrigation water go? An estimate of the contribution of irrigation to precipitation using MERRA. *J. Hydrometeor.*, **14**, 275–289, https://doi.org/10.1175/JHM-D-12-079.1.

Wurman, J., 2001: The DOW mobile multiple Doppler network. Preprints, *30th Int. Conf. on Radar Meteorology*, Munich, Germany, Amer. Meteor. Soc., 95–97.

——, and K. Kosiba, 2020: FARM-data-GRAINEX, version 1. Center for Severe Weather Research, accessed 15 December 2019, https://doi.org/10.48514/6XTH-M998.

——, and Coauthors, 2021: The Flexible Array of Radars and Mesonets (FARM). *Bull. Amer. Meteor. Soc.*, **102**, E1499–E1525, https://doi.org/10.1175/BAMS-D-20-0285.1.